Urban ventilation assessment with improved vertical wind profile in high-density cities – Investigations in nighttime extreme heat

Yueyang He [a,b], Chao Yuan [c,*], Chao Ren [d], Weiwen Wang [e,f], Yuan Shi [g], Edward Ng [a,b,h]

[a] *Institute of Future Cities, The Chinese University of Hong Kong, Hong Kong, China*
[b] *Institute of Environment, Energy and Sustainability, The Chinese University of Hong Kong, Hong Kong, China*
[c] *Department of Architecture, National University of Singapore, Singapore*
[d] *Division of Landscape Architecture, Faculty of Architecture, The University of Hong Kong, Hong Kong, China*
[e] *Institute for Environmental and Climate Research, Jinan University, Guangzhou, China*
[f] *Guangdong-Hong Kong-Macau Joint Laboratory of Collaborative Innovation for Environmental Quality, Guangzhou, China*
[g] *Department of Geography and Planning, University of Liverpool, Liverpool, UK*
[h] *School of Architecture, The Chinese University of Hong Kong, Hong Kong, China*

ARTICLE INFO

ABSTRACT

Climate change and heatwaves challenge urban dwellers' thermal comfort and health. In Hong Kong, more frequent and intensive extreme heat has been observed recently. This study uses Light Detection and Ranging (LiDAR) to observe vertical wind profiles and calibrate numerical simulation methods for urban ventilation assessment in nighttime extreme heat (i.e. hot nights (HNs)) at a high-density site. A cross-comparison is conducted to the characteristics between the observed HN-averaged wind profiles and commonly-used 24-h-period-averaged wind profiles in summer. The observation reveals a weaker wind environment in HNs than 24-h-periods, and the weakest condition is found in HNs during prolonged extreme heat where the impacts of weakened advection surpass enhanced thermal buoyancy. Furthermore, CFD simulations are conducted to evaluate the deviations on urban ventilation assessment caused by the lack of consideration of nighttime extreme heat when setting inlet wind profiles and site thermal conditions. In the simulation results, the 24-h-period-averaged wind profiles cause significant deviations on pedestrian-level wind speed and velocity ratio (empirical model (>45%); LiDAR observation (>20%)). Considerable deviations are found when unstable thermal stratification is ignored (>20%). Consistent deviations on vertical turbulent flow structures induced by the inexplicit coupling between thermal buoyancy and advection are found. The findings call for urgent attention to the wind conditions in HNs since they are most needed for releasing heat stress and urban overheating. It is recommended to include explicit buoyancy effects in both measurement and modeling works to optimize urban ventilation assessment for tackling extremely high-temperature and weak-wind conditions.

1. Introduction

1.1. Background

In tropical and subtropical climates, urban ventilation is important in promoting human thermal comfort and health as well as mitigating the Urban Heat Island (UHI) effects [1,2]. A previous study has suggested that every 1 m/s increase in wind speed can mitigate a 2 °C rise in urban air temperature in summer [3]. However, the urban wind environment is sensitive to its surrounding morphological features, especially in high-density cities [4,5]. Thus, continuous efforts have been made in high-density cities to establish and optimize urban ventilation assessment tools and relevant urban planning/design guidelines for designing a better-ventilated city and solving the weak-wind-related environmental problems [6–8].

The recent trend of global climate change presents a new challenge to urban ventilation assessment. According to the latest report of the Intergovernmental Panel on Climate Change (IPCC) in 2021, the global surface temperature is successively higher in each of the last four decades and it is likely to reach an additional increment of 0.5 °C earliest in 2030 if the current warming rate continues [9]. It is virtually certain that extreme heat, including heatwaves, have clearly discernible increases in

their frequency and intensity on most of the land regions [9]. They have been regarded as one of the major causes of heat-related mortality worldwide [10–14]. Worse still, cities intensify human-induced warming locally, and urbanization consequently increases the severity of these extreme heat [15–17]. Under this circumstance, a better understanding on how the wind behaves in extreme heat is required to support accurate urban ventilation assessment when the wind is most needed for heat-stress relief. Yet, the progress so far is hindered by the lack of field observation data and the complex heat-wind interactions in urban boundary layers [18].

1.2. A "new normal" in Hong Kong

As one of the most representative high-density cities, Hong Kong suffers from high-temperature and weak-wind conditions in summer. Additionally, in line with the recent trend of global climate change, Hong Kong Observatory (HKO) has observed a faster annual mean temperature rise [19]. Such changing climate has consequentially led to a substantial increase in local extreme heat, which can be identified by hot nights (HNs: daily minimum air temperature ≥ 28 °C [20]) and very hot days (HDs: daily maximum air temperature ≥ 33 °C [21]). For example, the number of HNs in the summer months (i.e. June to August) has gone up by 3 times from 2000 to 2020 (Fig. 1a). During these two decades, a total 45 HNs in maximum have been identified in summer 2020, constituting half of the entire summer (Fig. 1b). This upward increasing trend of extreme heat is expected to continue in the foreseeable future [22].

As extreme heat has become a "new normal" in Hong Kong, their impacts have aroused an emerging concern of local urban climate and heat-related mortality [23]. In a long-term study conducted by Ren et al. [24], extreme heat can enhance the typical UHI effects in Hong Kong by a 1.7 °C rise in intensity and a 59% increase in duration. With the enhanced UHI effects, the weak wind conditions in high-density cities tend to contribute more to higher mortality, as revealed by Goggins et al. [25]. Furthermore, extreme heat at nighttime was found to have stronger associations with excess mortality than those at daytime [23, 26]. Particularly, Wang et al. [23] attributed the highest mortality risks to prolonged extreme heat. Meanwhile, Shi et al. [27] investigated the spatial variability of extreme hot weather conditions in Hong Kong. Their regression models addressed the importance of urban ventilation for mitigating extreme heat, especially at the nighttime. The above findings suggest an urgent need of attentions to wind conditions in the "new normal" in Hong Kong, as well as a critical review on relevant urban ventilation assessment and wind-adaptive urban planning/design.

1.3. Research gaps and objectives

To address weak-wind-related urban problems and guide wind-adaptive urban planning/design, the Planning Department, Hong Kong SAR Government has established the Air Ventilation Assessment (AVA) system since 2006 [8]. AVA provides a systematic methodology to assess pedestrian-level wind conditions using either wind tunnel or Computational Fluid Dynamics (CFD) simulations. This methodology has been used in all major developments in Hong Kong [29], and applied into other high-density cities [30–33]. However, the AVA system needs a critical review and update since its existing vertical wind profile dataset, named "site wind availability data" [34], has two main limitations. Firstly, this dataset was developed by wind tunnel and mesoscale meteorological modeling, and has not been validated by field observation. Secondly, this dataset does not take into account the "new normal" wind conditions in summer. Particularly, a standard AVA test currently adopts 24-h-period-averaged wind data in either annual or seasonal extracts in this dataset to reproduce inflow boundary conditions regardless of extreme or non-extreme hot weather conditions. Therefore, a refinement of the dataset is needed to tackle the increasingly frequent and intense extreme heat such as HNs, where the wind is most needed for relieving heat-stress and potentially reducing heat-related mortality risks.

Based on Light Detection and Ranging (LiDAR) observation of vertical urban wind speed profiles, which is introduced in Section 2, we aim to address the above two limitations, by conducting two studies. The first study (another paper [35]) is conducted to address the first limitation, i.e. lack of validation, by evaluating the accuracy of wind profiles estimated by various conventional methods, including physical models (i.e. wind tunnel), mesoscale meteorological models, and empirical models (e.g. Power Law (PL)). The second study (the current paper) is conducted to address the second limitation, i.e. lack of consideration of extreme heat in summer, by two steps: 1) cross-comparison between the "new normal" (i.e. HN-averaged) and commonly-used (i.e. 24-hour-period-averaged) wind profiles; and 2) evaluation of the impacts of these wind profiles on the CFD-based thermally-stratified urban ventilation assessment results. Specifically, the HN-averaged LiDAR wind profiles are used as a benchmark for assessing the deviations caused by the 24-h-period-averaged wind profiles reproduced by LiDAR observation and a conventional method, respectively. In this paper, the PL (power law) wind profile method is selected as a representative conventional method to be evaluated since, compared to LiDAR observation, it is the optimal alternative, balancing accuracy and data availability to estimate neutrally-stratified wind profiles [35].
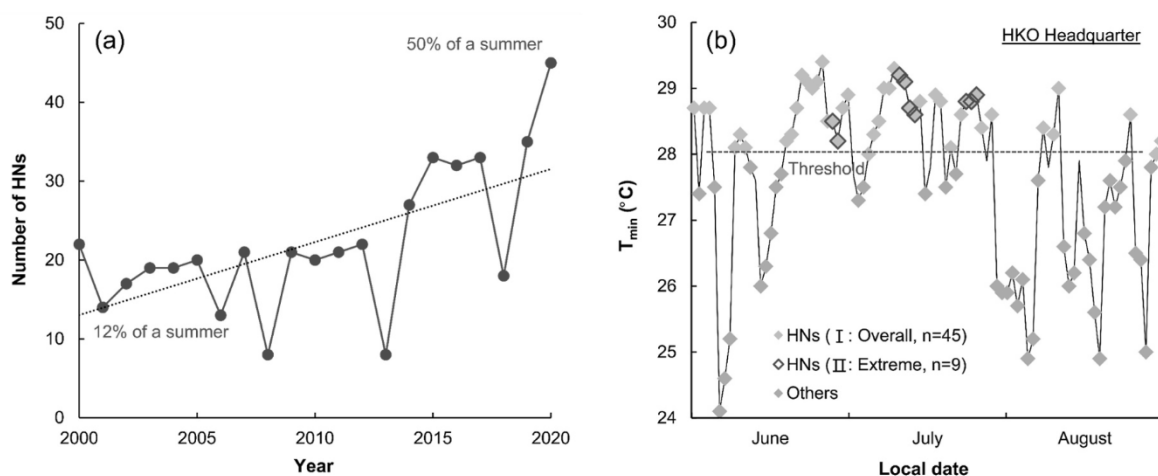

Fig. 1. Statistics of hot nights (HNs) in Hong Kong: (a) number of HNs in summer from 2000 to 2020; and (b) distribution of HNs in summer 2020 for overall situation (i.e. all HNs in summer 2020) and extreme situation (i.e. HNs in prolonged extreme heat as explained in Section 3) (source: HKO headquarter [28]).

2. Literature review on urban wind studies in extreme heat

Extreme heat are periods that trapped by abnormal warm air induced by synoptic-scale anticyclones [36]. Compared with non-extreme hot weather conditions in summer, extreme hot weather conditions further exacerbate the urban climate due to the amplified net radiation gain, increased anthropogenic heat, increased heat storage, decreased evapotranspiration, and decreased turbulent heat transport [37–40]. As one of the most complex urban climatic variables, wind in extreme heat is relatively weak due to the high-pressure circulation patterns under anticyclones [41]. Its behaviors have been increasingly studied by both field measurements and numerical simulations in recent years.

Based on conventional near-ground field measurements, a number of studies have revealed the positive contribution of wind to the synergies between heatwaves and UHI effects [42–44]. For example, in a study in Beijing during heatwaves, Li et al. [45] found that wind played different roles in the synergies during the daytime and nighttime. They suggested that wind speed had a stronger impact on the sensible heat flux in urban areas than the advection cooling effect from the rural areas during the daytime, while an opposite trend occurred during the nighttime. In a study in Seoul, Ngarambe et al. [46] found that UHI is more intense during heatwaves than non-heatwave, and these synergies between heatwaves and UHI were more obvious in densely built areas and under low wind speed conditions. In another study in Hong Kong, Zhang et al. [47] found that a larger background wind speed was associated with a faster increase in daily maximum air temperature at coastal urban areas during extreme heat.

More recently, the development of ground-based remote sensing technologies, such as wind LiDAR, provides a new and reliable method to measure vertical wind speed profiles in hot periods. For example, Wu et al. [48] launched a LiDAR observation on the upper-air wind behaviors in extreme heat at the metropolitan area of New York City. Their study presented a strong diurnal variation of boundary layer heights during heatwaves, as well as its associations with the transport of urban air pollution. Based on multi-point LiDAR, He et al. [49] observed the diurnal variation of summer vertical wind speed profiles in Hong Kong. Their results confirmed stronger buoyancy effects on the near-ground wind at the urban area with higher building density.

As for numerical simulations, mesoscale meteorological modeling has been widely used to predict urban surface wind and temperature in extreme heat [50–52]. As revealed by Li and Bou-Zeid [53], the low wind speed, together with the lack of surface moisture in urban areas, contributed the most to the enhanced UHI effects during extreme heat. Zhang et al. [54] quantified that the UHI effects can be reduced by over 25% during a heatwave if the upwind urban areas were replaced by natural vegetation in their simulations. Wang et al. [55] identified the different UHI circulation patterns over Beijing-Tianjing-Bebei region between the daytime and nighttime in the simulations. Furthermore, to understand the high-pressure atmospheric system induced by the UHI effects, Wang et al. [56] simulated the air circulation patterns under various background wind speed, heat flux and stratification conditions.

In microscales, CFD techniques have been widely used to simulate buoyancy-driven flow [57–59]. For example, based on unsteady Reynolds-averaged Navier-Stokes (URANS) and Large Eddy Simulation (LES) models, Mei and Yuan [60] investigated the merging of thermal plumes in an urban area of Singapore in calm conditions and attributed this phenomenon to both mean horizontal flow induced by pressure difference and turbulence induced by shear instability. Mei and Yuan [61] further conducted a literature review on buoyancy effects on urban ventilation, with a particular focus on strong buoyancy and weak wind conditions. Based on LES models, Wang et al. [62] investigated the coupled effects of mechanical and thermal turbulence with urban settings in Hong Kong and found that thermal turbulence enhanced pedestrian-level ventilation while thermal mixing was suppressed by high background wind speed. Besides, a few recent CFD studies have taken into account the near-ground wind and thermal conditions in

extreme heat. Amongst these studies, Toparlar et al. [40] used URANS models to analyze the effects of wind speed on urban surface temperature in Bergpolder Zuid during a heatwave. Antoniou et al. [63] conducted a validation study between URANS models and field measurements in terms of near-ground wind speed and temperature in four consecutive days of a heatwave in Nicosia.

Despite these studies, however, few studies have investigated the vertical wind distribution in extreme heat, especially at high-density urban areas. The lack of such understanding may lead to deviations on inflow boundary conditions in urban ventilation assessment in extreme heat, which finally results in mistaken assessment outputs and wrong decision making in urban planning/design.

3. Reproduction of vertical urban wind profiles at upwind

This section reproduces the abovementioned 24-h-period-averaged and HN-averaged vertical wind speed profiles in summer. A typical high-density urban site in Sai Wan, Hong Kong is selected as an example to reproduce the wind profiles. As shown in Fig. 2, the selected site is located at a downtown area of northwestern Hong Kong Island. It is characterized by inhomogeneous high-rise buildings and limited open spaces. Fig. 3 shows the spatial distribution of building heights at the site, where the maximum building height is around 180 m, and the ground coverage ratio is over 40%. The selected site has a relatively flat terrain, while mountains on the south bind it.

The 24-h-period-averaged and HN-averaged vertical wind speed profiles were reproduced by the following equations:

$$U_{\overline{24H}} = \frac{\sum_{i=1}^{m} U_{24H\_i}}{m} \tag{1}$$

$$U_{\overline{HN}} = \frac{\sum_{i=1}^{n} U_{HN\_i}}{n} \tag{2}$$

where $U_{\overline{24H}}$ and $U_{\overline{HN}}$ refer to the HN-averaged and 24-h-period-averaged wind speed at different measurement heights (Z), respectively; U_{24H_i} and U_{HN_i} refer to the hourly-averaged wind speed in each 24-h-period and HN at Z, respectively; and m and n refer to the number of the identified 24-h-periods and HNs during a study period, respectively. In this paper, following the AVA technical circular [29], $U_{\overline{24H}}$ was calculated by considering all 24-h-periods in summer regardless of extreme or non-extreme hot weather conditions, i.e., m = 92. In comparison, two types of $U_{\overline{HN}}$ were calculated: 1) $U_{\overline{HN}}$-I: by considering all 45 HNs (i.e., n = 45), as identified in Fig. 1b, in summer 2020; and 2) $U_{\overline{HN}}$-II: by extracting 9 HNs (i.e., n = 9, Fig. 1b) in the middle of prolonged extreme heat in a pattern of 2D3N (i.e. 3 consecutive HNs with 2 HDs in between) in summer 2020, as 2D3N has the strongest association with the amplified mortality risks among different patterns of prolonged extreme heat in Hong Kong [23]. The reproduction of the hourly-averaged vertical wind speed profiles was based on LiDAR observation or conventionally-used PL method, with further explanations in Sections 3.1 and 3.2.

3.1. LiDAR vertical urban wind profiles

The LiDAR method was based on a continuous field observation of vertical wind speed profiles on the roof-top of Yam Pak building in Hong Kong University at the selected site, as shown in Fig. 2. From the wind LiDAR, laser beams were emitted and received cyclically to detect the Doppler shifts (Δf) of the moving aerosol particles in the atmosphere:

$$\Delta f = f - f_0 \tag{3}$$

where f_0 refers to the frequency of the emitted laser beams, and f refers to the frequency of the laser beams backscattered by the particles. The detected Δf was converted into corresponding radical wind speed, and the radical wind speed at different azimuths and heights were used to
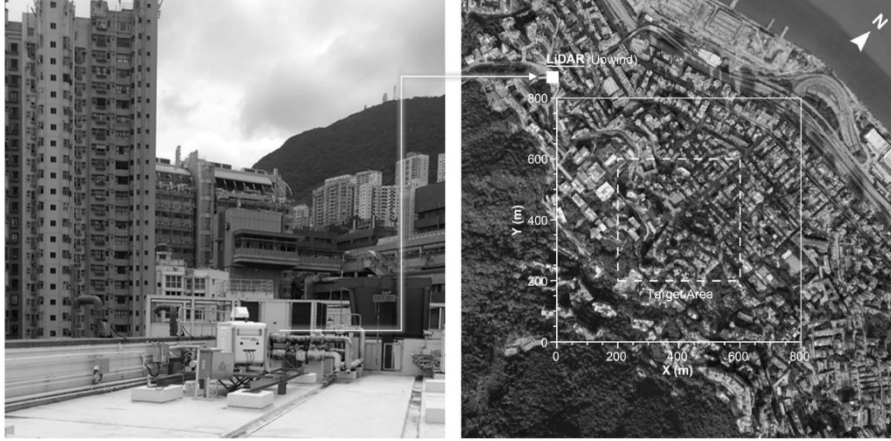
Fig. 2. Selected high-density urban site (800 m × 800 m) in Sai Wan, Hong Kong for reproducing vertical wind speed profiles, and the wind LiDAR location on top of the roof of Yam Pak building (15 m above the ground).
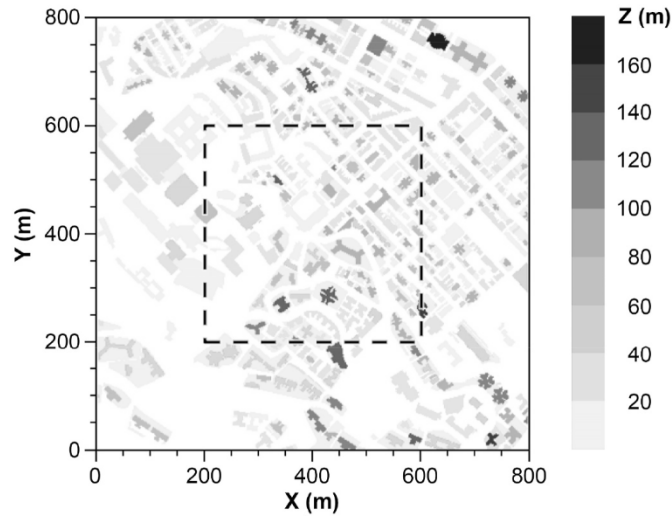

Fig. 3. Spatial distribution of building heights at the selected urban site in Sai Wan, Hong Kong.

reproduce vertical profiles of wind speed and direction. In this paper, the Doppler Beam Swinging (DBS) scan mode was used to reproduce the hourly-averaged LiDAR wind speed profiles:

$$U = \frac{\sqrt{(V_{RE} - V_{RW})^2 + (V_{RE} - V_{RS})^2}}{2 \sin \gamma} \tag{4}$$

where V_{RE}, V_{RW}, V_{RN} and V_{RS} refer to the radial wind speed along the east-tilted, west-tilted, north-tilted and south-tilted directions detected at each height above the test site (Fig. 2) in a DBS scan circle; and γ refers to the half cone angle between the vertical direction and the four tilted directions. A diagram to explain the principle of the DBS scan mode is attached in Appendix A. The observational data in summer 2020 was extracted in the prevailing southwest wind direction (i.e., $180° \leq \theta \leq 270°$) during non-typhoon periods. The extracted data was used to reproduce both the 24-h-period-averaged and HN-averaged wind profiles. Detailed settings of the wind LiDAR are listed in Table 1. On-site validation results of the wind LiDAR conducted at the King's Park meteorological station in Hong Kong based on the upper-air data from radiosondes [64] are shown in Appendix A.

Table 1
Settings of wind LiDAR for observing the vertical wind speed profile in summer 2020.

Instrument condition	Detailed setting
LiDAR model	WindCube 100S
Scan mode	Doppler beam swinging (DBS)
Scan range	50 m to 3 km above the scanner
Scan cycle	Approximately 20s
Range gate (i.e., discrete interval)	25 m
Half cone angle	15°
Laser beams wavelength	1.54 μm
Carrier-to-noise ratio	−27 dB [49]
Measurement accuracy	0.5 m/s of radial wind speed at the range between 0 and 115 m/s [65]

3.2. Power law vertical urban wind profile

The conventionally-used PL method reproduced the vertical wind speed profiles by integrating the site wind availability data [34] developed by Regional Atmospheric Modeling System (RAMS) modeling with the power law empirical formula as suggested in the AVA technical circular [29]. In this hybrid method, the site wind availability data provides the reference wind speed above a test site and the power law formula determines the shape of its wind profile. In this paper, the hourly-averaged PL wind speed profiles were extrapolated as:

$$U = U_\infty \left(\frac{Z}{Z_\infty} \right)^a \tag{5}$$

where U_∞ refers to the reference wind speed at the height of 500 m (Z_∞) from the computational cell (0.5 km × 0.5 km) covering the selected urban site (Fig. 2) in the RAMS dataset; and α refers to the power law index where 0.35 was assigned to represent the terrain roughness of a city center according to the widely-used AIJ recommendations [66]. Currently, only 24-h-period-averaged reference wind data in either annual or seasonal extracts are available in the RAMS dataset. Hence, this paper used the reference wind data in summer extract under the sector of southwest wind direction to reproduce the 24-h-period-averaged wind profile. Detailed settings of the RAMS model for developing the site wind availability data are listed in Table 2.

3.3. Cross-comparison of 24-h-period-averaged and HN-averaged vertical urban wind profiles

The 24-h-period-averaged and HN-averaged vertical wind speed

Table 2

Settings of RAMS model [67] for developing the site wind availability data.

Model condition	Detailed setting
Mesoscale model	RAMS (version 6.0)
Horizontal data resolution	12.5 km (outermost); 2.5 km (middle); 0.5 km (innermost)
Simulation time	Year 2000–2009
Topography	Actual terrain height
Land surface types	Land-use data in a latitude/longitude resolution of 400'' (outermost); 80'' (middle); and 16'' (innermost)
Nudging	Near-ground wind and temperature data from local automatic weather stations [28]
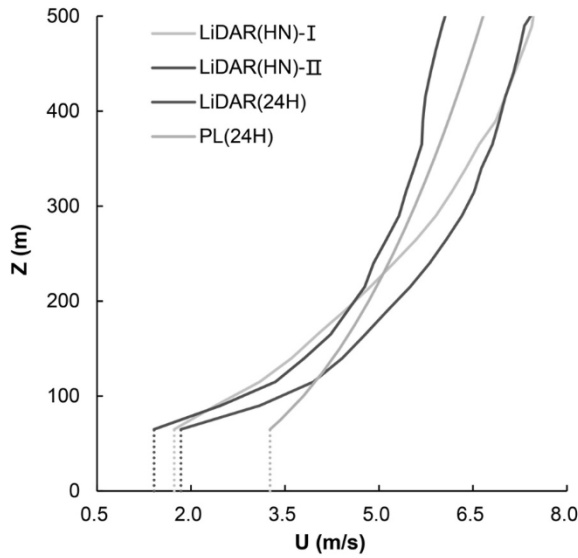
Fig. 4. Vertical wind speed (*U*) profiles reproduced by LiDAR observation and conventionally-used power law (PL) method in hot nights (HNs) or 24-h-periods (24Hs) in summer.

profiles from LiDAR in summer are plotted together for a cross-comparison in Fig. 4. The observation shows wind speed in hot nights, i.e. LiDAR(HN), is smaller than the one at 24-h-periods, i.e. LiDAR(24H). It suggests the needs of additional attentions to the weak wind conditions in nighttime extreme heat. Particularly, obviously smaller background wind speed (as indicated by U_∞) is observed in HNs in the extreme situation (HNs-II) than the overall situation (HNs-I). This phenomenon is mainly caused by the weaker advection under stronger high-pressure circulation patterns in prolonged extreme heat at the upwind. This weakened advection generates more significant impacts on the urban flow than the thermal buoyancy, and eventually cause smaller wind speed in HNs in prolonged extreme heat. In such a situation, urban thermal environment is exacerbated by heat-stress that lasts longer, while this heat-stress can be trapped inside street canyons due to the lower incoming wind speed [68]. Furthermore, the LiDAR results indicate the strong heat-wind interactions within the urban boundary layer

over a high-density urban site as the shapes of wind profiles vary significantly under different buoyancy effects. The strongest buoyancy effects are observed in the weakest wind condition in prolonged extreme heat, i.e. LiDAR(HN)- II, which is consistent with the previous findings [61]. However, these highly variable buoyancy-induced flow behaviors in the reality cannot be described by the power law wind profile, i.e. PL (24H).

4. CFD simulations

Based on the wind profiles reproduced in Section 3, this section used the LES model in an open-source CFD code, Parallelized LES Model (PALM) version 6.0, to conduct urban ventilation assessment. The LES model relies on filtered and incompressible Navier-Stokes equations in Boussinesq-approximated form [69], and explicitly resolves large and energy-containing eddies. The LES model has been validated in both neutral [35] and unstable [70] thermal conditions with high-density urban settings, and the descriptions of these validations and their results are attached in Appendix B. Test scenarios in CFD are defined in Section 4.1. Methods to set the inlet wind profiles and site thermal conditions in CFD are described in Sections 4.2 and 4.3, respectively.

4.1. Test scenarios in CFD

Eight test scenarios were defined, which included two benchmark scenarios and six parametric scenarios to be evaluated (Table 3). We considered nighttime extreme hot weather conditions (LiDAR(HN)) and unstable site thermal conditions (U) in two situations (overall (I) and extreme (II)) as two benchmark scenarios (LiDAR(HN)–U-I/II). The impacts of three types of parameters, i.e., 1) weather conditions (hot night (HN) and 24-h-period (24H)); 2) thermal conditions (neutral (N) and unstable (U)), and 3) measurement methods (PL and LiDAR), are evaluated in other six parametric scenarios, by comparing with the benchmark scenarios.

4.2. Settings of computational domain, grids and flow boundary conditions

The computational domain had a size of 2800 m (X) × 800 m (Y) × 500 m (Z) (Fig. 5), which refers to the recommendations on the minimum distances between buildings and domain boundaries by AIJ guidelines [35,71]. The computational gird was structured with a total cell number of 1400 (X) × 400 (Y) × 120 (Z), where the cell size was 2 m with no stretching ratio in the horizontal dimension and 1 m with a stretching ratio of 1.03 beyond the height of 25 m in the vertical dimension. This grid resolution was determined by a grid-sensitivity test conducted by Gronemeier et al. [72] in PALM, based on a high-density urban model, to best compromise simulation accuracy and computational cost.

In the computational domain, the inlet boundary prescribed the vertical wind speed profiles reproduced in Section 3. To have a fair cross-comparison, this paper only prescribed the vertical wind speed profiles within the range from 65 m to 500 m, where both LiDAR and PL methods' data are available. The wind speed below the height of 65 m at
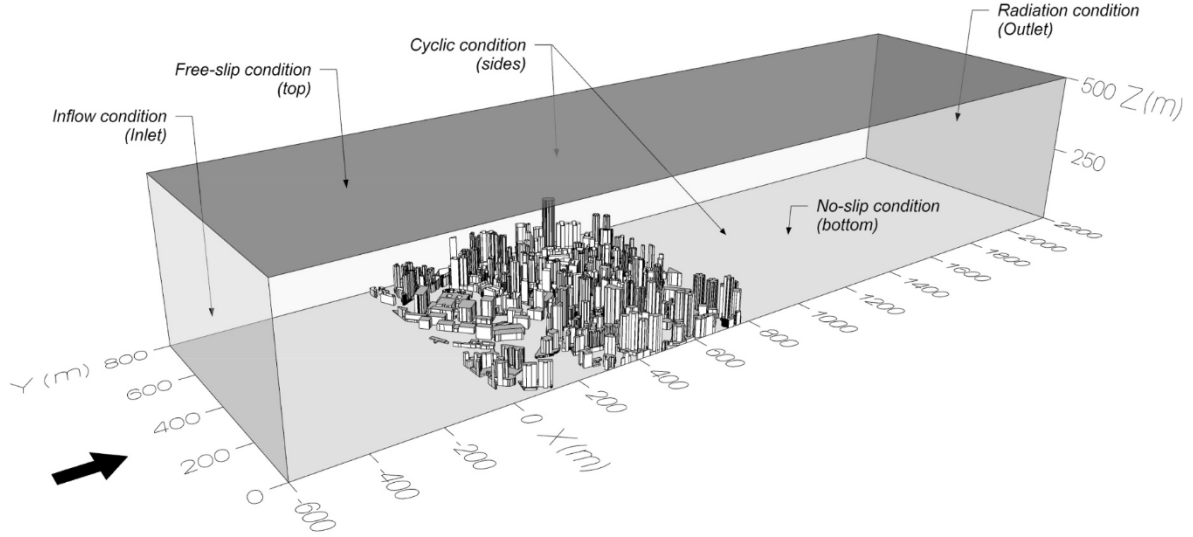
Table 3

Test scenario definitions with different input parameters for CFD simulations.

Scenarios	Methods	Weather conditions	Thermal conditions	Situations
LiDAR(HN)–U-I/II	LiDAR	Hot night (HN)	Unstable (U)	Overall (I)
PL(24H)–U-I/II	PL	24-h-period (24H)	Neutral (N)	Extreme (II)
LiDAR(24H)–U-I/II				
LiDAR(HN)–N-I/II				

Note: total eight test scenarios are involved with different combinations of four pairs of alternative input parameters, where "methods" and "weather conditions" prescribe inlet wind profiles; "thermal conditions" prescribe site thermal conditions; and "situations" determine the effects of HNs on both inlet wind profiles and site thermal conditions.

Fig. 5. Computational domain and boundary conditions of the LES model with a high-density urban model.

all the scenarios was prescribed to be constant. It assumed that the wind speed gradient inside urban canopies is negligible below the displacement height until quite close to the ground surface, referring to the descriptions in the reality by Bentham and Britter [73], and Oke [74]. Based on prescribed vertical wind speed profiles, the initial turbulence was generated by the synthetic turbulence generator [75], where the instantaneous wind speed component (u_i) at the inlet was calculated at each time step (t) by the following equation:

$$u_i(t) = \overline{u}_i(t) + \alpha_{ij}(t)u'_j(t) \qquad (6)$$

where $i, j \in \{1, 2, 3\}$; $\overline{u}_i$ refers to a mean wind speed component; α_{ij} refers to an amplitude tensor derived from the Reynolds stress tensor, which was parametrized automatically by the method of Rotach et al. [76] in PALM; and u'_j refers to the turbulent motions, which were obtained by the following equation:

$$u'_j(t) = u'_j(t - \Delta t)exp\left(\frac{-\pi\Delta t}{2T}\right) + \psi_j(t - \Delta t)\left[1 - exp\left(\frac{-\pi\Delta t}{T}\right)\right]^{0.5} \qquad (7)$$

where ψ_j refers to a set of random data generated independently in PALM at each time step, with a zero mean and a unity variance; Δt refers to the interval of 1 time step; and T refers to the Lagrangian time scale.

The outlet boundary adopted a radiation condition. The bottom, top and lateral boundaries adopted no-slip, free-slip and cyclic condition, respectively. The total simulation time for each scenario was 1.5 h, in which the simulation result in the last half hour was averaged and outputted. Automatic adjustment of the time step is set to guarantee the courant number less than 1.

4.3. Settings of urban thermal conditions

The LES model adopts either neutral (N) or unstable (U) thermal conditions to include the impacts of thermal buoyancy at the test urban site. The calculation of heat transfer was switched off, in the test scenarios with neutral thermal conditions (i.e., LiDAR(HN)–N-I/II). In the test scenarios with unstable thermal conditions (i.e., LiDAR(HN)–U-I/II, PL(24H)–U–I/II, and LiDAR(24H)–U-I/II), initial temperature was set to be homogeneous at the inlet and computational domain with reference to the averaged air temperature recorded at the automatic weather station at HKO headquarter [28] in hot summer nights, 2020. Specifically, the averaged maximum air temperature in all 45 HNs is 30.1 °C and 30.6 °C in the overall (I) and extreme situations (II), respectively. To activate the heat transfer and reproduce the convective flow field in the simulations, a constant flux layer was assumed as the boundary
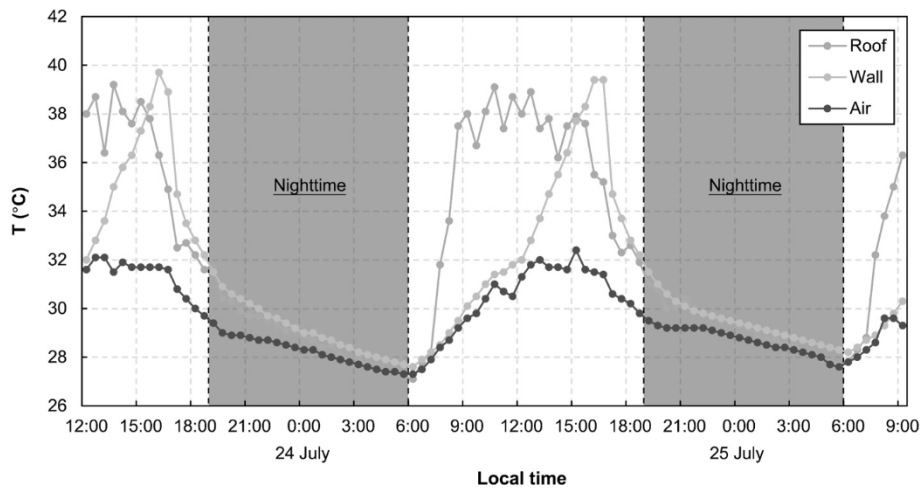

Fig. 6. Diurnal variations of surface (building roof and wall) and air temperature measured at Yam Pak building (Fig. 2) in Hong Kong University from 24 to 25 July in summer 2008 [77].

conditions of all building/ground surfaces.

The surface heat flux was set according to the field measurement data obtained at Yam Pak building (Fig. 2) by Yang and Li [77]. Fig. 6 shows the diurnal variations of surface temperature measured on the building roof and walls by thermal couples. Since a similar trend of surface temperature on the building roof and walls was observed at the nighttime, this paper assumed the heat flux from all building/ground surfaces was the same and estimated the kinematic sensible heat flux (H) based on the maximum nighttime temperature difference (i.e., around 1.7 °C) between the surfaces and ambient air:

$$H = \frac{h\left(T_{surface} - T_{air}\right)}{cp \bullet \rho} \tag{8}$$

where h refers to the convective heat transfer coefficient, which is assumed to be 12 W K^{-1} m^{-2} based on the numerical estimation in urban-like settings given by Awol et al. [78]; $T_{surface}$ and T_{air} refer to the surface and air temperature, respectively; and ρ refers to the density of dry air (1.225 kg m^{-3}). It should be noted that the minimum air temperature measured by the weather station on the building roof from 24 to July 25, 2008 is close to 28 °C, which is the threshold [20] to define a HN.

5. Results and discussion

This section cross-compares two benchmark scenarios and six parametric scenarios to investigate the impact of input wind profiles on CFD simulation results. Three pairs of input parameters, which are defined in Section 3, are cross-compared in this section: 1) conventionally-used wind profiles (i.e., PL) versus LiDAR wind profiles; 2) 24-h-period-averaged wind profiles versus HN-averaged wind profiles; and 3) neutral thermal conditions (N) versus unstable thermal conditions (U). The benchmark pairs are LiDAR(HN)–U-I/II. Sections 5.1 and 5.2 analyze the

pedestrian-level and upper-level wind speed respectively. Section 5.3 further analyzes the pedestrian-level wind velocity ratio, which is the ratio between pedestrian-level wind speed and reference-height wind speed.

5.1. Deviations of wind speed at the pedestrian level

5.1.1. Qualitative analysis

The pedestrian-level wind speed contours, simulated by CFD in different scenarios (Table 3), are plotted in Figs. 7 and 8. Overall, the inlet wind profiles and site thermal conditions in the parametric scenarios (i.e., PL(24H)–U-I/II, LiDAR(24H)–U-I/II, and LiDAR(HN)–N-I/II) cause significant deviations on the assessment of pedestrian-level wind speed in HNs. Particularly, these deviations are more significant in the extreme situation (II), which focuses on HNs in prolonged extreme heat, than the overall situation (I).

Conventionally-used wind profiles (PL) versus LiDAR wind profiles (benchmark): Based on the benchmark scenarios with LiDAR observation, the conventionally-used (PL) wind profiles, i.e. PL(24H)–U-I/II, lead to significant overestimations of pedestrian-level wind speed in HNs. The overestimations can be explained by two reasons. Firstly, the power law formula itself has deficiencies to explicitly describe the shapes of wind profiles, which are highly modified by urban heterogeneities and buoyancy effects [79,80]. Secondly, the mesoscale meteorological modeling dataset (i.e. site wind availability data), which provides reference wind speed to the PL wind profiles [29], cannot precisely extract U_∞ in HNs. In this paper, the mesoscale meteorological model underestimates U_∞ in HNs in the overall situation (i.e. summer), and overestimates U_∞ in HNs in the extreme situation (i.e. prolonged extreme heat) as revealed in Fig. 4.

24-h-period-averaged wind profiles versus HN-averaged wind profiles (benchmark): Overestimations of pedestrian-level wind speed in HNs are also induced by the 24-h-period-averaged profiles even though
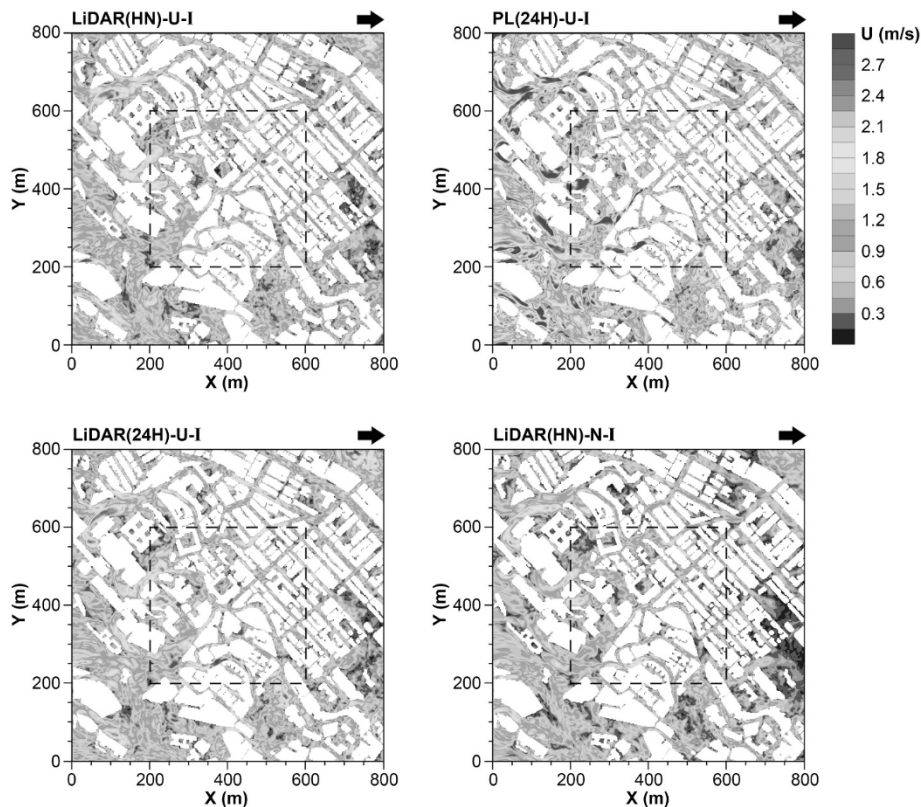

Fig. 7. Pedestrian-level distributions (Z = 2 m) of wind speed (*U*) in four scenarios (Table 3) in overall situation (I): hot nights (HNs) in summer. LiDAR(HN)–U-I is the benchmark scenario.
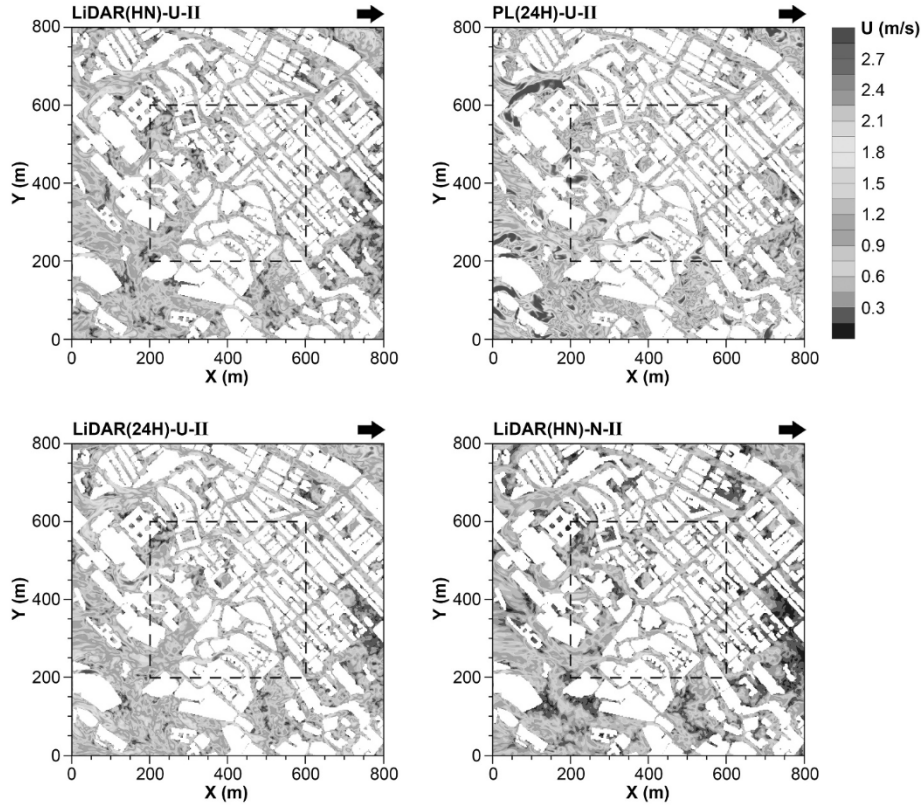
Fig. 8. Pedestrian-level distributions (Z = 2 m) of wind speed (*U*) in four scenarios (Table 3) in extreme situation (II): hot nights (HNs) in prolonged extreme heat. LiDAR (HN)–U-II is the benchmark scenario.

the LiDAR Technology was used, i.e., LiDAR(24H)–U-I/II, although they are less significant than those induced by the conventionally-used PL wind profiles (i.e., PL(24)-U-I/II). Overall, the deviations are mainly because the LiDAR observation in 24-h-periods fails to specify the buoyancy effects in HNs, which can significantly modify the shapes of the upwind wind profiles (Fig. 4). In the HNs in prolonged extreme heat (II), the deviation is also caused by the 24-h-period-averaged LiDAR data because of the overestimation of the advection and incoming wind scale.

Neutral thermal conditions versus unstable thermal conditions (benchmark): The neutral thermal conditions, i.e. LiDAR(HN)–N-I/II, which ignore buoyancy effects at the test site, cause underestimations of pedestrian-level wind speed in HNs. This phenomenon confirms the effects of urban heating on boundary layer climate as descripted by Oke [37]. A similar result has been described by a previous study [60], which revealed a considerable enhancement on pedestrian-level wind speed by the buoyancy effects in high-density urban areas in nighttime calm conditions.

5.1.2. Quantitative analysis

More than the qualitative analysis, we used two indicators, the percentage deviation of wind speed (PD_U) and percentage deviation of wind speed frequency (PD_F), to quantify the deviations on urban ventilation assessment caused by the inlet wind profiles and site thermal conditions which are lack of consideration of nighttime extreme heat. PD_U and PD_F are calculated as:

$$PD_U = \frac{U_{Evaluation} - U_{Benchmark}}{U_{Benchmark}} \times 100\% \qquad (9)$$

$$PD_F = \frac{F_{Evaluation} - F_{Benchmark}}{F_{Benchmark}} \times 100\% \qquad (10)$$

where $U_{Evaluation}$ and $U_{Benchmark}$ refer to the spatially-averaged wind speed from CFD simulations in the benchmark scenarios and the

parametric scenarios to be evaluated, respectively. Correspondingly, $F_{Evaluation}$ and $F_{Benchmark}$ refer to the frequency of the simulated wind speed in the benchmark scenarios and the parametric scenarios to be evaluated, respectively. The calculation of the two indicators was conducted at the central target area of 400 m (X) × 400 m (Y) of the test site (Figs. 7 and 8) to consider the impacts of immediate surroundings and minimize the impacts of recirculating flow at the downwind cavity zone.

The results of PD_U at the pedestrian level are shown in Fig. 9. The largest deviations are caused by the conventionally-used (PL) wind profiles, i.e. PL(24H)–U-I/II, which overestimate over 30% and 45% of
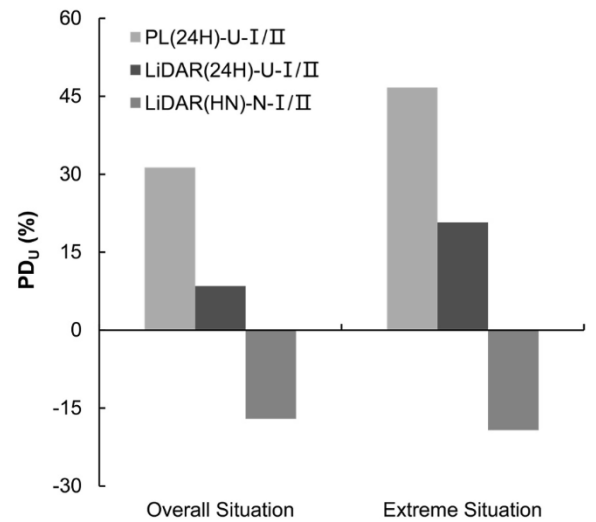

Fig. 9. Percentage deviation of pedestrian-level wind speed (PD_U) of different scenarios in overall situation (I): hot nights (HNs) in summer; and extreme situation (II): HNs in prolonged extreme heat.

pedestrian-level wind speed in HNs in the overall (i.e. summer) and extreme (i.e. prolonged extreme heat) situations, respectively. These deviations are larger than those caused by the inexplicit representation of mechanical effects of urban roughness at the same high-density site by the PL method (i.e. around 25% [35]). The larger deviations in the current paper suggest that the accuracy of conventional methods for assessing pedestrian-level wind can be further reduced if the thermal effects in extreme heat (e.g. HNs) are not specified. Besides, smaller but still significant deviations are seen when using either the 24-h-period-averaged LiDAR wind profiles, i.e. LiDAR(24H)–U-I/II, or the neutral thermal conditions, i.e. LiDAR(HN)–N-I/II. They either overestimate or underestimate pedestrian-level wind speed by over 20%. This result quantitatively reveals the deviations on pedestrian-level wind assessment caused by the improper use of LiDAR observational data.

Furthermore, the results of PD_F are given by categorizing the simulated pedestrian-level wind speed into three ranges: comfort (>1.3 m/s), medium (0.3–1.3 m/s), and poor (≤0.3 m/s). This criterion [81] was established to evaluate the influence of wind speed on outdoor thermal comfort based on the surveys conducted by Cheng et al. [82] and Ng et al. [83] in Hong Kong. As shown in Fig. 10, based on the simulations results, obvious deviations are seen at both the comfort and poor zones. Among the scenarios, the conventionally-used (PL) wind profiles cause the largest deviations of over 190%, and the deviations caused by the 24-h-period-averaged LiDAR wind profiles and neutral thermal conditions are over 80%. These large deviations suggest the importance of explicit consideration of buoyancy effects in pedestrian-level wind assessment for addressing outdoor thermal comfort.

5.2. Deviations of wind speed at the upper level

5.2.1. Qualitative analysis

The stream-wise (along X dimension) wind speed distributions in the vertical dimension are shown in Figs. 11 and 12. The analysis mainly focuses on the upper levels till around 200 m, covering the urban canopy layer in Hong Kong (0–60 m [84]), and the highest buildings at the test site (around 180 m). Based on the benchmark scenarios, i.e. LiDAR(HN)–U-I/II, the deviations caused by the inlet wind profiles or site thermal conditions in the parametric scenarios (i.e., PL(24H)–U-I/II, LiDAR(24H)–U-I/II, and LiDAR(HN)–N-I/II) are as follows:

Conventionally-used wind profiles versus LiDAR wind profiles (benchmark): The conventional (PL) method, i.e. PL(24H)–U-I/II, largely overestimates the mean flow within and just above the urban

canopy layer in HNs. Consequently, the conventional method causes deviations when predicting both the mechanical and thermal effects on turbulent motions from urban morphologies since these effects are sensitive to the incoming flow at high-density urban areas [62]. Particularly, in the extreme situation where prolonged extreme heat occurs, the conventional method causes even larger deviations on the mean flow and turbulent motions due to the stronger buoyancy effects and weaker incoming wind conditions in the reality.

24-h-period-averaged wind profiles versus HN-averaged wind profiles (benchmark): The 24-h-period-averaged LiDAR wind profiles, LiDAR(24H)–U-I/II, which do not specify the effects of thermal buoyancy and advection at the upwind in HNs, also overestimate the mean flow and turbulent motions in the vertical wind assessment. The 24-h-period-averaged LiDAR wind profiles cause stronger and more intense vertical mixing within and just above the urban canopy layer, because they obtain larger enhancements from the thermal effects at the upwind.

Neutral thermal conditions versus unstable thermal conditions (benchmark): the neutral thermal conditions, i.e. LiDAR(HN)–N-I/II, which do not take into account the buoyancy effects at the site in HNs, lead to less vertical mixing within the urban canopy layer and more laminar flow structure above the layer than the observation by LiDAR. The result reveals the deficiency of the neutral thermal conditions on reproducing the unstably-stratified vertical wind distributions under extreme hot weather conditions at a high-density urban site. It is consistent with some previous findings on urban boundary layer flow [70,72]. To indicate the vertical distribution of buoyancy effects at the site in HNs, the simulated spatially-averaged vertical profiles of temperature difference of the two benchmark scenarios are attached in Appendix C.

5.2.2. Quantitative analysis

The simulated wind speed at the upper levels (i.e., 0–240 m) above the target area are quantitatively compared by PD_U, as depicted in Fig. 13. Similar as the results at the pedestrian level, the inlet wind profiles or site thermal conditions in the parametric scenarios lead to more obvious deviations in the extreme situation (i.e. prolonged extreme heat) than the overall situation (i.e. summer) in HNs. The largest deviations are seen within the urban canopy layer, where the scenarios based on the conventional (PL) method, i.e. PL(24H)–U-I/II, cause the deviations of over 45%, and the scenarios based on LiDAR observation, i.e. LiDAR(24H)–U-I/II and LiDAR(HN)–N-I/II, cause the deviations of over 25%. These large deviations may cause misleading
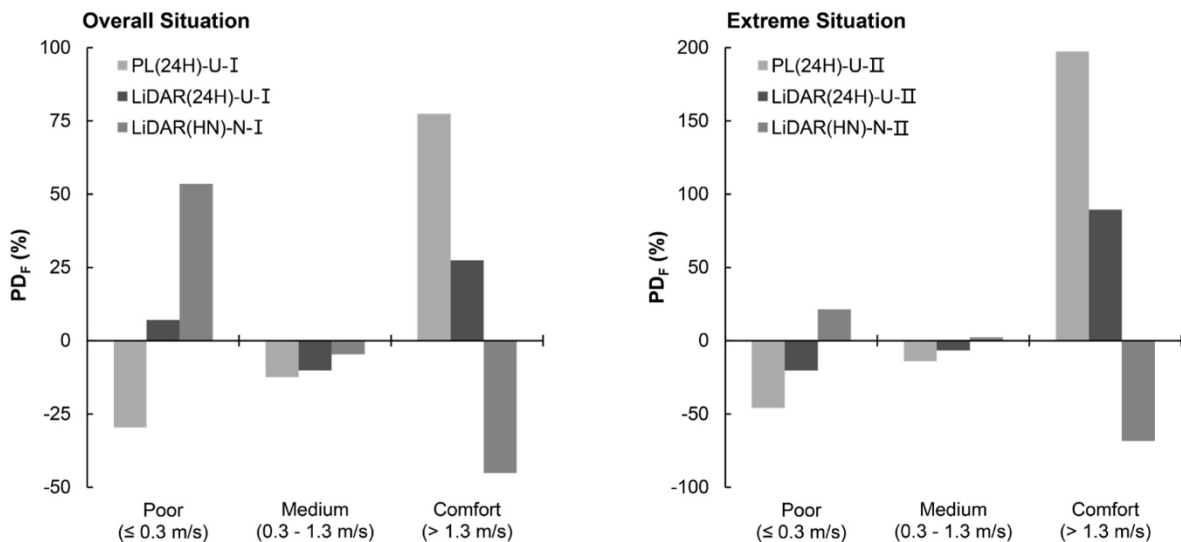

Fig. 10. Percentage deviation of pedestrian-level wind speed frequency (PD_F) at three ranges of wind comfort [81] of different scenarios in overall situation (I): hot nights (HNs) in summer; and extreme situation (II): HNs in prolonged extreme heat.
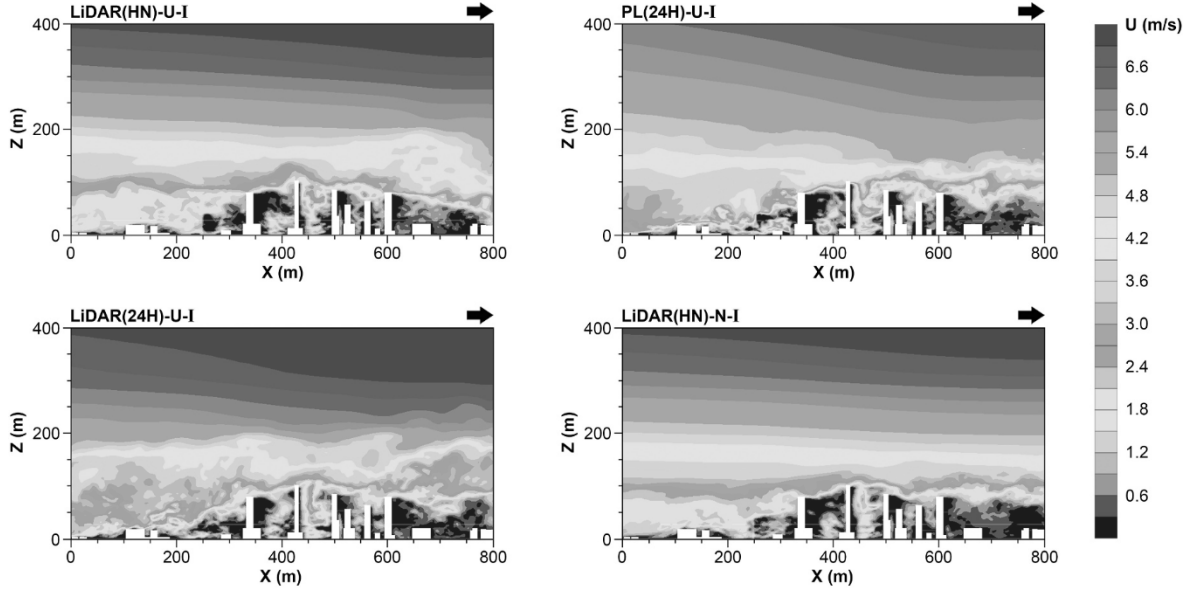
Fig. 11. Vertical distributions (Y = 400 m) of wind speed (*U*) along prevailing southwest wind direction in four scenarios (Table 3) in overall situation (I): hot nights (HNs) in summer. LiDAR(HN)–U-I is the benchmark scenario.
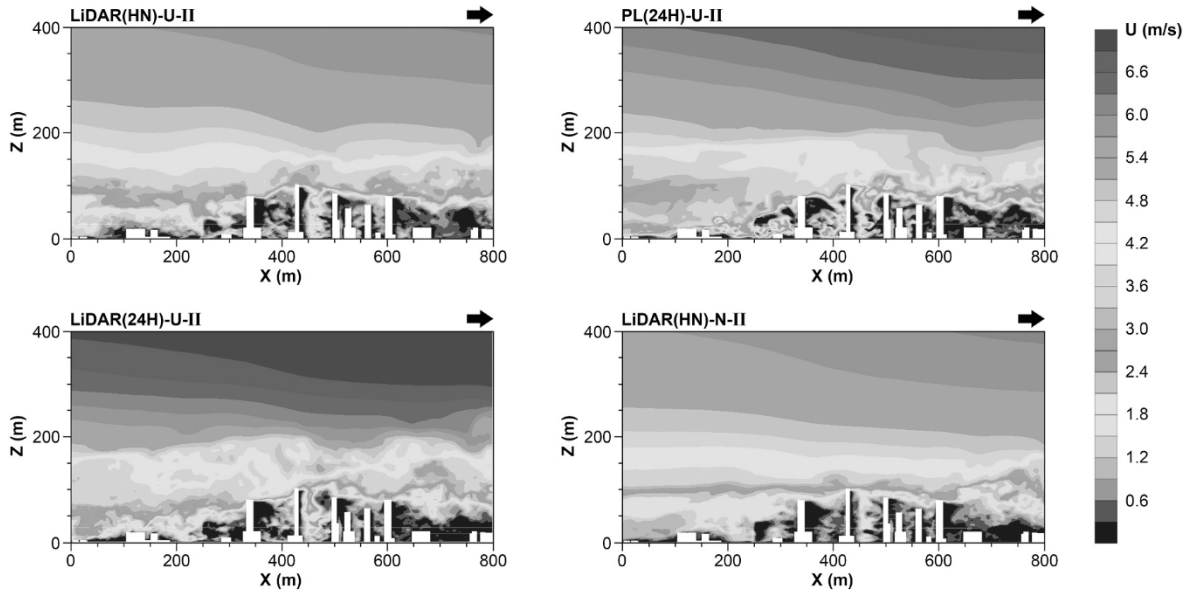

Fig. 12. Vertical distributions (Y = 400 m) of wind speed (*U*) along prevailing southwest wind direction in four scenarios (Table 3) in extreme situation (II): hot nights (HNs) in prolonged extreme heat. LiDAR (HN)–U-II is the benchmark scenario.

results in upper-level wind assessment inside street canyons, especially the deep ones, where the heat can be easily trapped at nighttime [68]. They may also mislead the other assessment associated with the outdoor wind field, such as the assessment of outdoor pollutant dispersion and indoor natural ventilation.

5.3. Deviations of wind velocity ratio at the pedestrian level

In addition to the analysis of wind speed, we converted wind speed into wind velocity ratio (*VR*) to indicate the wind availability at different heights of the test site by the following equation:

$$VR = \frac{U}{U_\infty} \tag{11}$$

where *U* refers to the simulated wind speed at an evaluation height; and

U_∞ refers to the upwind wind speed at the height of 500 m (Fig. 4). The simulated spatially-averaged vertical *VR* profiles of different scenarios over the target area are shown in Fig. 14. Compared with wind speed, *VR* describes more clearly the shape characteristics of wind profiles modified by both of the mechanical and thermal effects since *VR* excludes the impacts of different incoming wind scales (as indicated by U_∞). Thus, *VR* is currently used as the indicator in AVA as required by the technical circular [29].

Based on the simulated *VR*, we used an indicator, the percentage deviation of wind velocity ratio (PD_{VR}), to quantify the deviations on pedestrian-level wind assessment caused by the inlet wind profiles and site thermal conditions. PD_{VR} is calculated as:

$$PD_{VR} = \frac{VR_{Evaluation} - VR_{Benchmark}}{VR_{Benchmark}} \times 100\% \tag{12}$$
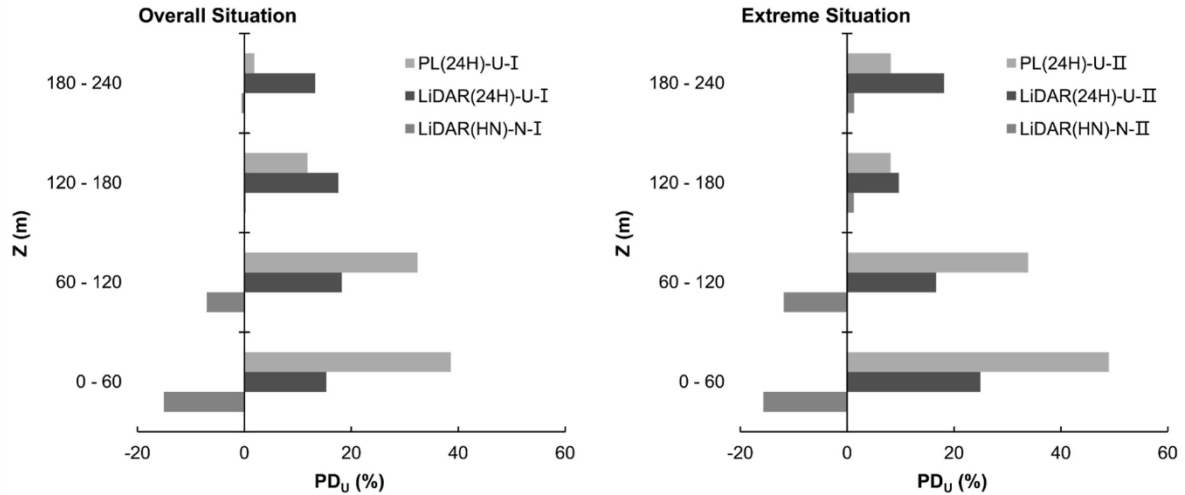
Fig. 13. Percentage deviation of wind speed (PD_U) at upper levels (0–240 m) of different scenarios in overall situation (I): hot nights (HNs) in summer; and extreme situation (II): HNs in prolonged extreme heat.
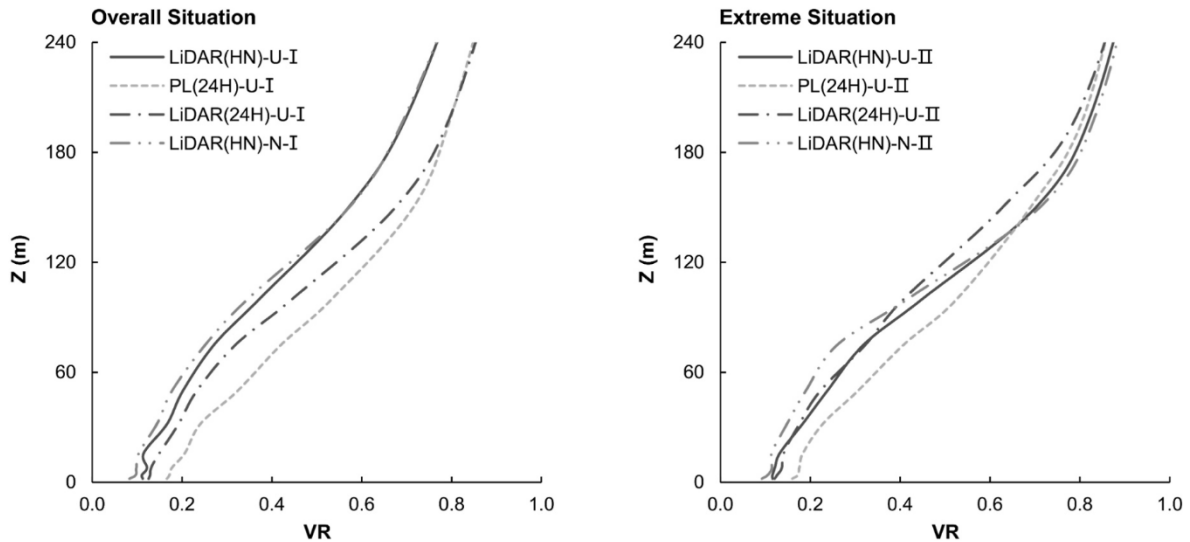

Fig. 14. Simulated spatially-averaged vertical wind velocity ratio (*VR*) profiles at upper levels (0–240 m) of different scenarios in overall situation (I): hot nights (HNs) in summer; and extreme situation (II): HNs in prolonged extreme heat (note: *VR* excluded the impacts of U_∞ of different scenarios and focused on the impacts of their profile shapes).

where $VR_{Evaluation}$ and $VR_{Benchmark}$ refer to the *VR* at the pedestrian level from CFD in the benchmark scenarios (i.e. LiDAR(HN)–U-I/II) and the parametric scenarios to be evaluated, respectively.

The distributions of PD_{VR} of different scenarios to be evaluated are depicted in Fig. 15. The largest deviations are seen in the scenarios using the conventional (PL) wind profiles (i.e. PL(24H)–U-I/II). These deviations are more obviously distributed at the zones with larger open spaces. Furthermore, the spatially-averaged deviations caused by different input parameters are summarized in Fig. 16: over 45% by the PL wind profiles (i.e. PL(24H)–U-I/II); around 10% by the 24-h-period-averaged LiDAR wind profiles (i.e. LiDAR(24H)–U-I/II); and over 20% by the neutral thermal conditions (i.e. LiDAR(HN)–N-I/II). Different from the results of PD_U at the pedestrian level in Section 4.1.2, which indicate larger deviations in the extreme situation (i.e. prolonged

extreme heat) than the overall situation (i.e. summer), an opposite trend is seen in the results of PD_{VR}. Particularly, in the extreme situation, PD_U caused by the 24-h-period-averaged LiDAR wind profile is over 20% (Fig. 9), while the results of PD_{VR} turn out to be negligible.

On one hand, the larger deviation on pedestrian-level wind speed is attributed to the different U_∞ between 24-h-periods and HNs in prolonged extreme heat, as confirmed in Fig. 4. On the other hand, the smaller deviation on pedestrian-level *VR* suggests that the buoyancy effects of modifying the shapes of wind profiles are comparable between 24-h-periods and HNs in prolonged extreme heat, as confirmed in Fig. 14. Despite that the 24-h-period-averaged LiDAR wind profile only causes small PD_{VR}, it still causes a large deviation on the wind speed field in HNs, due to the inexplicit coupling effects between vertical mixing induced by thermal buoyancy and horizontal flow induced by advection.
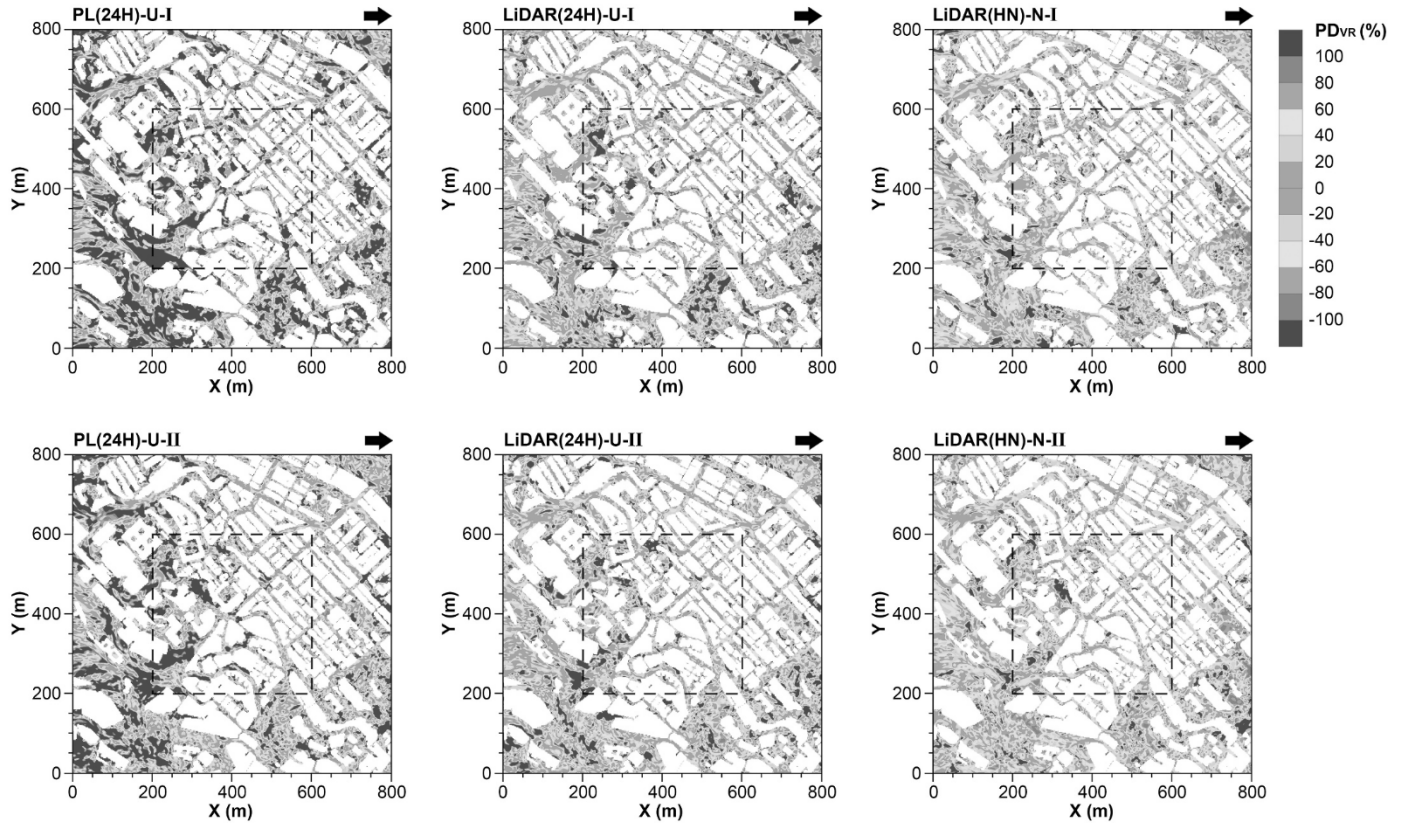
Fig. 15. Pedestrian-level distributions (Z = 2 m) of percentage deviation of wind velocity ratio (PD_{VR}) of different scenarios in overall situation (I): hot nights (HNs) in summer; and extreme situation (II): HNs in prolonged extreme heat (note: VR excluded the impacts of U_∞ of different scenarios and focused on the impacts of their profile shapes).
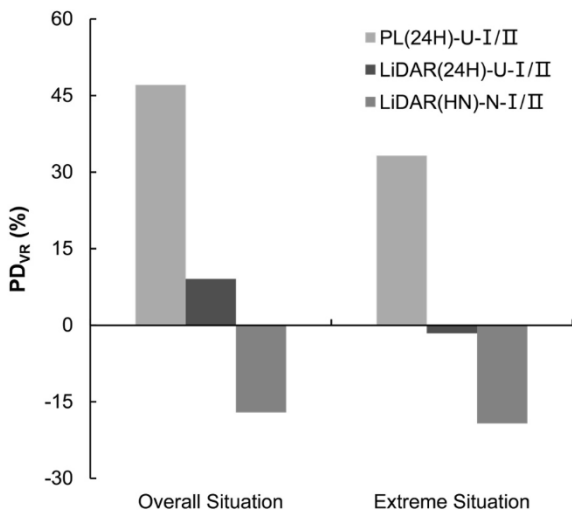

Fig. 16. Percentage deviation of pedestrian-level wind velocity ratio (PD_{VR}) in hot nights (HNs) of different scenarios in overall situation (I): HNs in summer; and extreme situation (II): HNs in prolonged extreme heat (note: VR excluded the impacts of U_∞ of different scenarios and focused on the impacts of their profile shapes).

All the quantitative results from Sections 5.1 to 5.3 are summarized in Table 4, including PD_U, PD_F, and PD_{VR} of the six parametric scenarios against the benchmark scenarios.

6. Conclusion

This study uses LiDAR observation to investigate the vertical wind profiles and calibrate numerical simulation methods for urban ventilation assessment in nighttime extreme heat in summer at a typical high-density urban area in Hong Kong. The observation in HNs involves two situations: 1) overall situation (i.e. HNs in summer); and 2) extreme situation (i.e. HNs in prolonged extreme heat). They are cross-compared with the observation in 24-h-periods for identifying the impacts of nighttime extreme heat on wind. Based on the observational data, CFD simulations with LES model are conducted to evaluate the deviations of urban ventilation assessment caused by the lack of consideration of nighttime extreme heat. Three pairs of input parameters are compared in CFD: 1) conventionally-used power law (PL) wind profile versus LiDAR wind profiles; 2) 24-h-period-averaged wind profile versus HN-averaged wind profiles; and 3) neutral thermal conditions versus unstable thermal conditions. Major findings are summarized and discussed on two aspects. Firstly, this study establishes a better understanding of wind conditions in high-density cities in nighttime extreme heat:

- Based on LiDAR observation, this study reveals weaker urban wind conditions in HNs than 24-h-periods in summer (Fig. 4). It means that urban dwellers suffer from not only higher-than-normal air temperature but also lower-than-normal wind speed in nighttime extreme heat.
- Particularly, the weakest pedestrian-level urban wind environment is found in HNs during prolonged extreme heat. This result indicates the impacts of the weakened advection are stronger than the enhanced thermal buoyancy under stronger high-pressure circulation patterns in prolonged extreme heat. Consequently, HNs in

Table 4
Summary of the percentage deviations of wind speed (PD_U), wind speed frequency (PD_F), and wind velocity ratio (PD_{VR}) of the six parametric scenarios. LiDAR(HN)–U-I/II are the benchmark scenarios.

Scenarios	PD_U (2 m)	PD_F (2 m, comfort zone)	PD_U (0–60 m)	PD_{VR} (2 m)
PL(24H)–U-I/II	>45%	>190%	>45%	>45%
LiDAR(24H)–U-I/II	>20%	>80%	>25%	>9%
LiDAR(HN)–N-I/II	< −20%	< −45%	< −15%	< −20%

prolonged extreme heat exacerbate urban thermal environment and lead to deteriorating heat-related health issues in Hong Kong [85].

- The current findings call for more attentions to the wind conditions in high-density cities in nighttime extreme heat given that they are weaker than the averaged wind conditions in summer, and crucial for releasing heat-stress and urban overheating.

Secondly, this study provides recommendations to improve the current methodology in AVA to address the impacts of nighttime extreme heat on urban ventilation:

- The conventional methods, e.g. PL (power law) method, to reproduce vertical wind speed profiles causes significant deviations on pedestrian-level wind speed (>45%) and wind speed frequency (>190%) in HNs (Figs. 9 and 10). These deviations are larger than those induced by the inexplicit representation of urban roughness in neutral thermal conditions by the PL method (i.e. wind speed (>25%); and wind speed frequency (>100%) [35]). It suggests the importance to carefully consider both mechanical effects and thermal effects in urban boundary layers when conducting urban ventilation assessment.
- Alternatively, the LiDAR observation to reproduce vertical wind speed profiles is more accurate. However, it is recommended to address the influence of specific thermal conditions on the flow at both the upwind (via measurements of wind profiles) and the test site (via simulations of thermal buoyancy) when assessing the pedestrian-level wind in HNs. Otherwise, considerable deviations are caused (wind speed (>20%); and wind speed frequency (>70%)) (Figs. 9 and 10).
- For AVA, the conventional methods should be used after optimization when assessing urban wind environments in extremely high-temperature and weak-wind conditions at nighttime. For example, when using the PL method, a more explicit classification of power law index can be established to better fit the LiDAR observation under different hot weather conditions. Otherwise, significant deviations are caused on the assessment of pedestrian-level *VR* (>45%) (Fig. 16) as well as the unstable vertical flow structure induced by the coupling effects between thermal buoyancy and advection (Figs. 11 and 12).
- To support more accurate AVA, the existing site wind availability data in Hong Kong should be refined. Given the significant deviations on pedestrian-level *VR* between HNs and 24-h-periods (>45%) (Fig. 16), the existing dataset, which only provides 24-h-period-averaged wind data, should be updated to tackle the extreme heat, such as HNs and HDs [20,21], where the wind is most needed for heat-stress relief. As such, a more advanced and real-time mesoscale meteorological model, such as the Weather Research and Forecasting (WRF) Model, with validation of long-term multi-point LiDAR observational data is required.

The different heat-wind relationships revealed in this study imply the needs of categorical understanding on the wind conditions under diverse hot periods. It is particularly important to better understand and assess the wind behaviors in high-density cities in nighttime extreme heat in summer given that they become excessive and are highly associated with public health. A better understanding and assessment of the "new normal" wind conditions are crucial for developing wind-adaptive urban planning/design strategies for a healthier and more comfortable living environment.

7. Limitations and future works

This paper only investigates the extreme heat at nighttime, while a subsequent investigation will be needed to tackle the situations at daytime, where wind conditions are expected to be more unstable due to the stronger buoyancy effects induced by solar radiation. Secondly, the paper only involves a typical urban site, while more urban areas and building densities should be studied in the future in order to diversify the buoyancy effects on urban ventilation. In addition, the paper only conducts urban ventilation assessment by CFD methods while such assessment should be repeated by physical methods in wind tunnel tests with thermal conditions being involved.

CRediT authorship contribution statement

Yueyang He: Writing – original draft, Software, Methodology, Investigation, Conceptualization. **Chao Yuan:** Writing – review & editing, Supervision, Methodology, Conceptualization. **Chao Ren:** Writing – review & editing, Methodology, Funding acquisition. **Weiwen Wang:** Software, Methodology. **Yuan Shi:** Software, Methodology. **Edward Ng:** Writing – review & editing, Supervision, Methodology, Funding acquisition, Conceptualization.

Declaration of competing interest

The authors declare that they have no known competing financial interests or personal relationships that could have appeared to influence the work reported in this paper.

Acknowledgement
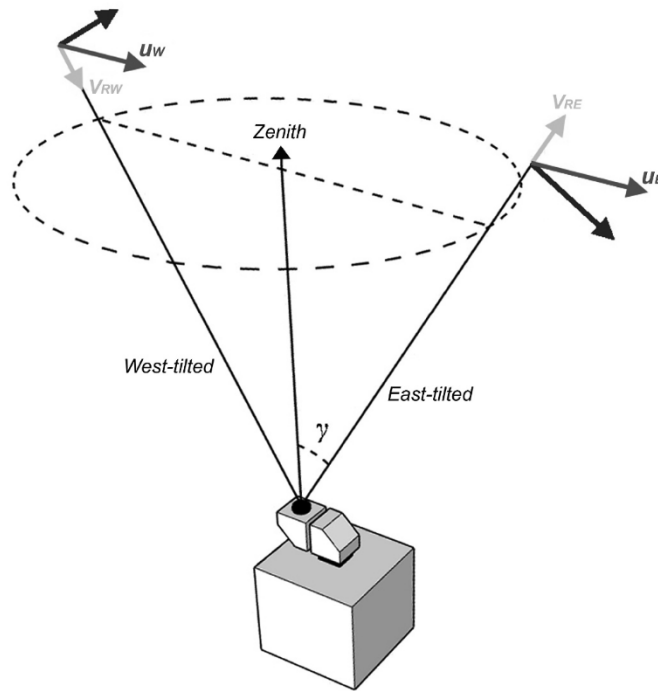
Appendix A. LiDAR scan mode and validation

Fig. 17. A DBS scan mode emits and receives at five directions, namely, the east-tilted, south-tilted, west-tilted, north-tilted and vertical directions in a circle. The diagram illustrates the radial wind speed to be detected along the east-tilted (V_{RE}) and west-tilted (V_{RW}) directions, as well as their conversions into the east-west horizontal component of wind speed ($u_{EW} = 0.5(V_{RE} - V_{RW})/sin\gamma$).
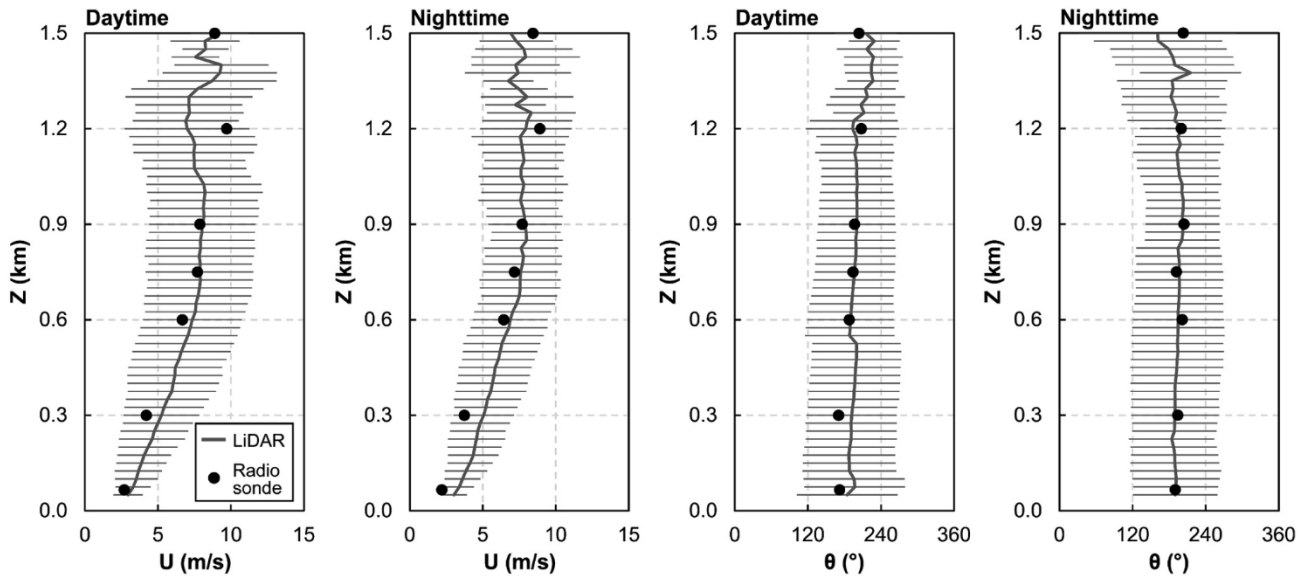
Fig. 18. Comparison of nighttime/daytime vertical profiles of horizontal wind speed (U) and direction (θ) (i.e., mean and standard deviations) measured by radiosondes and a wind LiDAR at the King's Park meteorological station at 8 a.m. and 8 p.m. daily [64] in a period of two weeks, where the overall R^2 reaches 0.88 and 0.82 for U and θ, respectively. The validation results confirm consistently high reliability of the LiDAR observational data at both the daytime and nighttime.

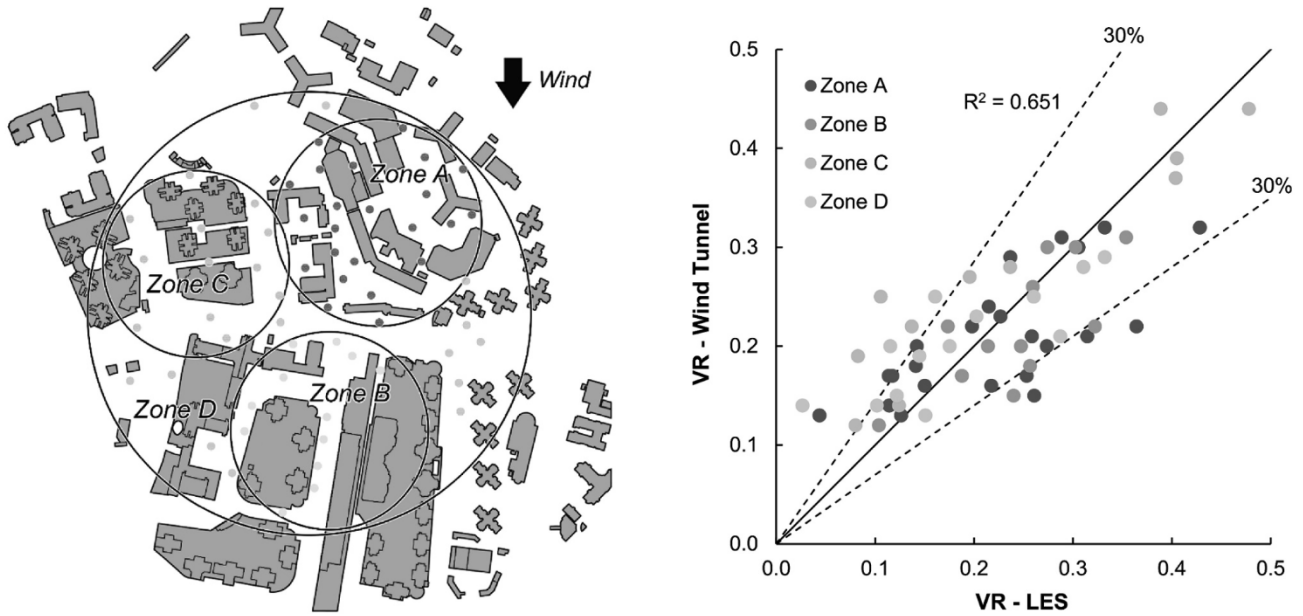## Appendix B. LES validations in neutral and unstable thermal conditions

Fig. 19. The current LES model on pedestrian-level wind velocity ratio (*VR*) in neutral thermal conditions has been validated by wind tunnel experimental data [86] at a high-density urban site in Sai Kung, Hong Kong under the northwest wind direction. In the experiment, the pedestrian-level wind speed was measured by multiple omni-directional sensors at a low-speed wind tunnel with a 1:400 reduced-scale urban model. The inlet wind speed at the gradient height was used to convert the pedestrian-level wind speed into *VR*. The inlet wind profile and urban model used in the experiment was input in the simulations to output urban wind field. The validation results based on 60 test points show the overall R^2 reaching around 0.65 and the root mean square error reaching around 0.06, which are in line with the previous validation results with high-density urban settings by PALM [70,87,88]. Despite the significant quantitative disagreements at some specific test points, the current LES model is able to achieve reliable understanding of spatially-averaged wind performance at high-density urban areas. More details of this validation can be found at [35].
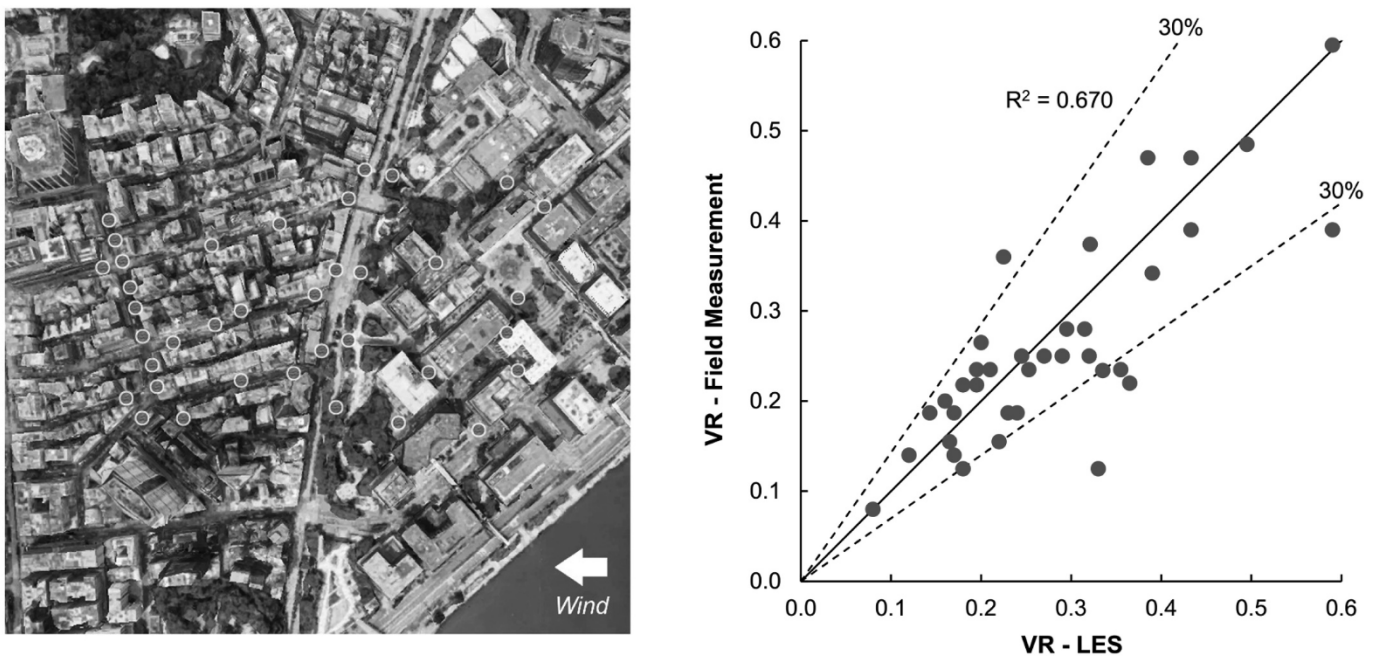

Fig. 20. The current LES model on pedestrian-level wind velocity ratio (*VR*) in unstable thermal conditions has been validated by Wang and Ng [70] based on a field measurement dataset [89] at a high-density urban site in Tsim Sha Tsui, Hong Kong under the east wind direction. In the field measurement, the pedestrian-level wind speed was recorded synchronously by twelve researchers with mobile air flow probes at multiple spots along six routes on a sunny and hot afternoon in 2006. Meanwhile, the instant upwind wind speed at Waglan Island automatic weather station [28] was recorded to convert the pedestrian-level wind speed into *VR*. To reproduce the effects of unstable thermal stratification on urban wind field in the LES model, homogeneous initial temperature was set at the inlet and domain with reference to the local meteorological data; and heat transfer between urban surfaces and ambient air was prescribed by kinematic heat flux determined in a sensitivity test. The validation results based on 37 measurement spots indicate the overall R^2 reaching 0.67, which is comparable to the validation results obtained in neutral thermal conditions [70]. More details of this validation can be found at [70].

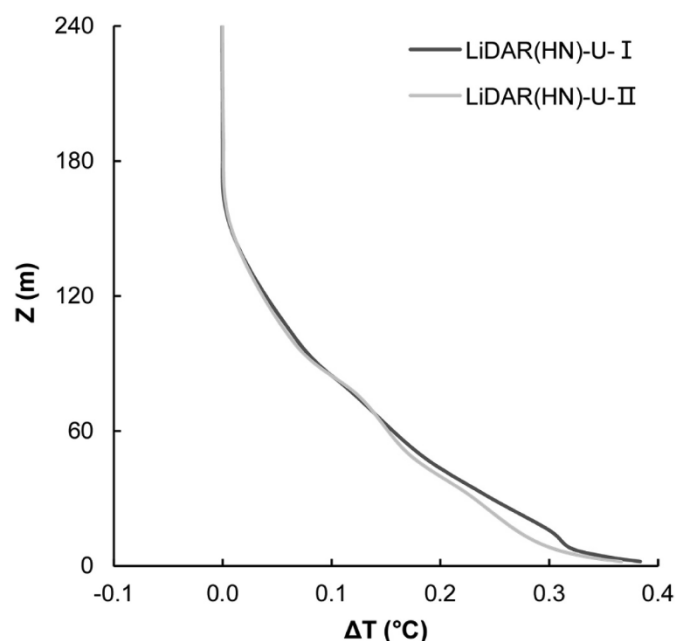## Appendix C. Vertical profiles of temperature

Fig. 21. Simulated spatially-averaged vertical profiles of temperature difference (ΔT) at upper levels (0–240 m) with HN-averaged LiDAR wind profiles in overall situation: HNs in summer; and extreme situation: HNs in prolonged extreme heat. According to the results, the buoyancy effects decrease gradually from the pedestrian level to the upper levels till around 180 m.

References

[1] B. Blocken, W. Janssen, T. van Hooff, CFD simulation for pedestrian wind comfort and wind safety in urban areas: general decision framework and case study for the Eindhoven University campus, Environ. Model. Software 30 (2012) 15–34.

[2] P. Höppe, The physiological equivalent temperature-a universal index for the biometeorological assessment of the thermal environment, Int. J. Biometeorol. 43 (2) (1999) 71–75.

[3] V. Cheng, E. Ng, C. Chan, B. Givoni, Outdoor thermal comfort study in a sub-tropical climate: a longitudinal study based in Hong Kong, Int. J. Biometeorol. 56 (1) (2012) 43–56.

[4] Y. He, A. Tablada, N.H. Wong, Effects of non-uniform and orthogonal breezeway networks on pedestrian ventilation in Singapore's high-density urban environments, Urban Clim. 24 (2018) 460–484.

[5] Y. He, A. Tablada, N.H. Wong, A parametric study of angular road patterns on pedestrian ventilation in high-density urban areas, Build. Environ. 151 (2019) 251–267.

[6] BCA, Ventilation Simulation Methodology and Requirements, BCA Green Mark Certification Standard for New Buildings, Building and Construction Authority (BCA), Singapore, 2012.

[7] MOE, Outline of the Policy Framework to Reduce Urban Heat Island Effects, Ministry of the Environment (MOE), Japan, 2004.

[8] E. Ng, Policies and technical guidelines for urban planning of high-density cities-air ventilation assessment (AVA) of Hong Kong, Build. Environ. 44 (7) (2009) 1478–1488.

[9] IPCC, Summary for Policymakers. in: Climate Change 2021: the Physical Science Basis. Contribution of Working Group I to the Sixth Assessment Report of the Intergovernmental Panel on Climate Change, Cambridge University Press, 2021.

[10] R. García-Herrera, J. Díaz, R.M. Trigo, J. Luterbacher, E.M. Fischer, A review of the European summer heat wave of 2003, Crit. Rev. Environ. Sci. Technol. 40 (4) (2010) 267–306.

[11] C. Heaviside, S. Vardoulakis, X.-M. Cai, Attribution of mortality to the urban heat island during heatwaves in the West Midlands, UK, Environ. Health 15 (1) (2016) 49–59.

[12] M. Nitschke, G.R. Tucker, A.L. Hansen, S. Williams, Y. Zhang, P. Bi, Impact of two recent extreme heat episodes on morbidity and mortality in Adelaide, South Australia: a case-series analysis, Environ. Health 10 (1) (2011) 1–9.

[13] P.J. Robinson, On the definition of a heat wave, J. Appl. Meteorol. Climatol. 40 (4) (2001) 762–775.

[14] T.T. Smith, B.F. Zaitchik, J.M. Gohlke, Heat waves in the United States: definitions, patterns and trends, Climatic Change 118 (3) (2013) 811–825.

[15] A. Lemonsu, V. Viguie, M. Daniel, V. Masson, Vulnerability to heat waves: impact of urban expansion scenarios on urban heat island and heat stress in Paris (France), Urban Clim. 14 (2015) 586–605.

[16] G.A. Meehl, C. Tebaldi, More intense, more frequent, and longer lasting heat waves in the 21st century, Science 305 (5686) (2004) 994–997.

[17] J. Tan, Y. Zheng, X. Tang, C. Guo, L. Li, G. Song, X. Zhen, D. Yuan, A.J. Kalkstein, F. Li, The urban heat island and its impact on heat waves and human health in Shanghai, Int. J. Biometeorol. 54 (1) (2010) 75–84.

[18] J.F. Barlow, Progress in observing and modelling the urban boundary layer, Urban Clim. 10 (2014) 216–240.

[19] G.M. Abbas, I.G. Dino, The Impact of Natural Ventilation on Airborne Biocontaminants: a Study on COVID-19 Dispersion in an Open Office, Construction and Architectural Management, Engineering, 2021.

[20] HKO, Number of hot nights observed at the Hong Kong Observatory since 1884 [cited 2021 July 15]; Available from: https://www.hko.gov.hk/en/cis/statistic/hngtday_statistic.htm, 2021.

[21] HKO, Number of very hot days observed at the Hong Kong Observatory since 1884 [cited 2021 July 15]; Available from: https://www.hko.gov.hk/en/cis/statistic/vhotday_statistic.htm, 2021.

[22] HKO, Climate projections for Hong Kong [cited 2021 8 Feb]; Available from: https://www.hko.gov.hk/en/climate_change/proj_hk_temp.htm, 2019.

[23] D. Wang, K.K.-L. Lau, C. Ren, W.B.I. Goggins, Y. Shi, H.C. Ho, T.-C. Lee, L.-S. Lee, J. Woo, E. Ng, The impact of extremely hot weather events on all-cause mortality in a highly urbanized and densely populated subtropical city: a 10-year time-series study (2006-2015), Sci. Total Environ. 690 (2019) 923–931.

[24] C. Ren, K. Wang, Y. Shi, Y.T. Kwok, T. Morakinyo, T.-c. Lee, Y. Li, Investigating the urban heat and cool island effects during extreme heat events in high density cities A case study of Hong Kong from 2000-2018, Int. J. Climatol. 41 (15) (2021) 6736–6754.

[25] W.B. Goggins, E.Y. Chan, E. Ng, C. Ren, L. Chen, Effect modification of the association between short-term meteorological factors and mortality by urban heat islands in Hong Kong, PLoS One 7 (6) (2012), e38551.

[26] H.C. Ho, K.K.-L. Lau, C. Ren, E. Ng, Characterizing prolonged heat effects on mortality in a sub-tropical high-density city, Hong Kong, Int. J. Biometeorol. 61 (11) (2017) 1935–1944.

[27] Y. Shi, C. Ren, M. Cai, K.K.-L. Lau, T.-C. Lee, W.-K. Wong, Assessing spatial variability of extreme hot weather conditions in Hong Kong: a land use regression approach, Environ. Res. 171 (2019) 403–415.

[28] HKO, Climatological database [cited 2021 July 15]; Available from: https://www.hko.gov.hk/en/cis/climat.htm, 2021.

[29] HPLB and ETWB, *Technical Circular No. 1/06: Air Ventilation Assessments.* 2006, Housing, Planning and Lands Bureau (HPLB) and Environment, Transport and Works Bureau(ETWB), Hong Kong SAR Government Hong Kong.

[30] NUS, Urban Climatic Mapping Studies for Singapore, 2021 [cited 2021.

[31] RAIA, The Lord Mayor's Brisbane buildings that breathes [cited 2021; Available from: https://www.architecture.com.au/archives/, 2021.

[32] C. Ren, R. Yang, C. Cheng, P. Xing, X. Fang, S. Zhang, H. Wang, Y. Shi, X. Zhang, Y.T. Kwok, Creating breathing cities by adopting urban ventilation assessment and

wind corridor plan-the implementation in Chinese cities, J. Wind Eng. Ind. Aerod. 182 (2018) 170–188.

[33] H. Tieben, J. Chu, N. Soares, E. Yiu, Environmental Urban design and planning rules and their impact on street spaces in Hong Kong and Macau, in: Proceedings of the 8th Conference International Forum on Urbanism, True Smart and Green City, Citeseer, 2015.

[34] PlanD, Site wind availability data [cited 2021 July 15]; Available from: https ://www.pland.gov.hk/pland_en/info_serv/site_wind/index.html, 2019.

[35] Y. He, C. Yuan, C. Ren, E. Ng, Urban Ventilation Assessment with Improved Vertical Wind Profile in High-Density Cities - Comparisons between LiDAR and Conventional Methods, publication process, 2022.

[36] E. Xoplaki, J.F. González-Rouco, J. Luterbacher, H. Wanner, Mediterranean summer air temperature variability and its connection to the large-scale atmospheric circulation and SSTs, Clim. Dynam. 20 (7–8) (2003) 723–739.

[37] T.R. Oke, Boundary Layer Climates, Routledge, 2002.

[38] C.D. Rogers, A.J. Gallant, N.J. Tapper, Is the urban heat island exacerbated during heatwaves in southern Australian cities? Theor. Appl. Climatol. 137 (1) (2019) 441–457.

[39] T. Sun, S. Kotthaus, D. Li, H.C. Ward, Z. Gao, G.-H. Ni, C.S.B. Grimmond, Attribution and mitigation of heat wave-induced urban heat storage change, Environ. Res. Lett. 12 (11) (2017), 114007.

[40] Y. Toparlar, B. Blocken, P.v. Vos, G. Van Heijst, W. Janssen, T. van Hooff, H. Montazeri, H. Timmermans, CFD simulation and validation of urban microclimate: a case study for Bergpolder Zuid, Rotterdam, Build. Environ. 83 (2015) 79–90.

[41] E. Gutiérrez, J.E. González, A. Martilli, R. Bornstein, M. Arend, Simulations of a heat-wave event in New York City using a multilayer urban parameterization, J. Appl. Meteorol. Climatol. 54 (2) (2015) 283–301.

[42] D. Founda, M. Santamouris, Synergies between urban heat island and heat waves in athens (Greece), during an extremely hot summer (2012), Sci. Rep. 7 (1) (2017) 1–11.

[43] H.S. Khan, R. Paolini, M. Santamouris, P. Caccetta, Exploring the synergies between urban overheating and heatwaves (HWs) in western Sydney, Energies 13 (2) (2020) 470.

[44] P. Ramamurthy, J. Gonzalez, L. Ortiz, M. Arend, F. Moshary, Impact of heatwave on a megacity: an observational analysis of New York City during July 2016, Environ. Res. Lett. 12 (5) (2017), 054011.

[45] D. Li, T. Sun, M. Liu, L. Wang, Z. Gao, Changes in wind speed under heat waves enhance urban heat islands in the Beijing metropolitan area, J. Appl. Meteorol. Climatol. 55 (11) (2016) 2369–2375.

[46] J. Ngarambe, J. Nganyiyimana, I. Kim, M. Santamouris, G.Y. Yun, Synergies between urban heat island and heat waves in Seoul: the role of wind speed and land use characteristics, PLoS One 15 (12) (2020), e0243571.

[47] C. Zhang, Q. Wang, P.W. Chan, C. Ren, Y. Li, The effect of background wind on summertime daily maximum air temperature in Kowloon, Hong Kong, Build. Environ. (2021) 108693.

[48] Y. Wu, K. Zhao, J. Huang, M. Arend, B. Gross, F. Moshary, Observation of heat wave effects on the urban air quality and PBL in New York City area, Atmos. Environ. 218 (2019), 117024.

[49] Y. He, C. Ren, H.W.L. Mak, C. Lin, Z. Wang, J.C.H. Fung, Y. Li, A.K.H. Lau, E. Ng, Investigations of high-density urban boundary layer under summer prevailing wind conditions with Doppler LiDAR: a case study in Hong Kong, Urban Clim. 38 (2021), 100884.

[50] C. Heaviside, X.M. Cai, S. Vardoulakis, The effects of horizontal advection on the urban heat island in Birmingham and the West Midlands, United Kingdom during a heatwave, Q. J. R. Meteorol. Soc. 141 (689) (2015) 1429–1441.

[51] L.E. Ortiz, J.E. Gonzalez, W. Wu, M. Schoonen, J. Tongue, R. Bornstein, New York City impacts on a regional heat wave, J. Appl. Meteorol. Climatol. 57 (4) (2018) 837–851.

[52] P. Ramamurthy, D. Li, E. Bou-Zeid, High-resolution simulation of heatwave events in New York City, Theor. Appl. Climatol. 128 (1–2) (2017) 89–102.

[53] D. Li, E. Bou-Zeid, Synergistic interactions between urban heat islands and heat waves: the impact in cities is larger than the sum of its parts, J. Appl. Meteorol. Climatol. 52 (9) (2013) 2051–2064.

[54] D.L. Zhang, Y.X. Shou, R.R. Dickerson, Upstream urbanization exacerbates urban heat island effects, Geophys. Res. Lett. 36 (24) (2009).

[55] Q. Wang, C. Zhang, C. Ren, J. Hang, Y. Li, Urban heat island circulations over the Beijing-Tianjin region under calm and fair conditions, Build. Environ. 180 (2020), 107063.

[56] Q. Wang, J. Hang, Y. Fan, Y. Li, Urban plume characteristics under various wind speed, heat flux, and stratification conditions, Atmos. Environ. 239 (2020), 117774.

[57] J. Allegrini, V. Dorer, J. Carmeliet, Buoyant flows in street canyons: validation of CFD simulations with wind tunnel measurements, Build. Environ. 72 (2014) 63–74.

[58] R. Priyadarsini, W.N. Hien, C.K.W. David, Microclimatic modeling of the urban thermal environment of Singapore to mitigate urban heat island, Sol. Energy 82 (8) (2008) 727–745.

[59] C. Yuan, A.S. Adelia, S. Mei, W. He, X.-X. Li, L. Norford, Mitigating intensity of urban heat island by better understanding on urban morphology and anthropogenic heat dispersion, Build. Environ. 176 (2020), 106876.

[60] S.-J. Mei, C. Yuan, Three-dimensional simulation of building thermal plumes merging in calm conditions: turbulence model evaluation and turbulence structure analysis, Build. Environ. 203 (2021), 108097.

[61] S.-J. Mei, C. Yuan, Urban buoyancy-driven air flow and modelling method: a critical review, Build. Environ. (2021), 108708.

[62] W. Wang, X. Wang, E. Ng, The coupled effect of mechanical and thermal conditions on pedestrian-level ventilation in high-rise urban scenarios, Build. Environ. 191 (2021), 107586.

[63] N. Antoniou, H. Montazeri, M. Neophytou, B. Blocken, CFD simulation of urban microclimate: validation using high-resolution field measurements, Sci. Total Environ. 695 (2019), 133743.

[64] HKO, Upper-air weather measurements in Hong Kong [cited 2021 July 15]; Available from: https://www.hko.gov.hk/en/wservice/tsheet/uamet.htm, 2021.

[65] Vaisal, Wind energy WindCube [cited 2021 8 Feb]; Available from: https://www. vaisala.com/en/wind-lidars/wind-energy/windcube, 2021.

[66] AIJ, AIJ Recommendations for Loads on Buildings, Architectural Institute of Japan (AIJ), Japan, 1996.

[67] PlanD, Final Report: Site Wind Availability System and Web-Based Site Wind Availability Database, Consultancy Study on Establishment of Simulated Site Wind Availability Data for Air Ventilation Assessments in Hong Kong, Planning Department, Hong Kong SAR government (PlanD), Hong Kong, 2013.

[68] N.H. Wong, K.J. Steve, Air temperature distribution and the influence of sky view factor in a green Singapore estate, J. Urban Plann. Dev. 136 (3) (2010) 261–272.

[69] B. Maronga, S. Banzhaf, C. Burmeister, T. Esch, R. Forkel, D. Fröhlich, V. Fuka, K. F. Gehrke, S. Geletič, S. Giersch, Overview of the PALM model system 6.0, Geosci. Model Dev. (GMD) 13 (3) (2020) 1335–1372.

[70] W. Wang, E. Ng, Air ventilation assessment under unstable atmospheric stratification-A comparative study for Hong Kong, Build. Environ. 130 (2018) 1–13.

[71] Y. Tominaga, A. Mochida, R. Yoshie, H. Kataoka, T. Nozu, M. Yoshikawa, T. Shirasawa, AIJ guidelines for practical applications of CFD to pedestrian wind environment around buildings, J. Wind Eng. Ind. Aerod. 96 (10–11) (2008) 1749–1761.

[72] T. Gronemeier, S. Raasch, E. Ng, Effects of unstable stratification on ventilation in Hong Kong, Atmosphere 8 (9) (2017) 168.

[73] T. Bentham, R. Britter, Spatially averaged flow within obstacle arrays, Atmos. Environ. 37 (15) (2003) 2037–2043.

[74] T.R. Oke, Initial Guidance to Obtain Representative Meteorological Observations at Urban Sites, Instruments and Observing Methods, World Meteorological Organization, 2004. *Report No. 81*.

[75] Z.-T. Xie, I.P. Castro, Efficient generation of inflow conditions for large eddy simulation of street-scale flows, Flow, Turbul. Combust. 81 (3) (2008) 449–470.

[76] M.W. Rotach, S.E. Gryning, C. Tassone, A two-dimensional Lagrangian stochastic dispersion model for daytime conditions, Q. J. R. Meteorol. Soc. 122 (530) (1996) 367–389.

[77] L. Yang, Y. Li, City ventilation of Hong Kong at no-wind conditions, Atmos. Environ. 43 (19) (2009) 3111–3121.

[78] A. Awol, G.T. Bitsuamlak, F. Tariku, Numerical estimation of the external convective heat transfer coefficient for buildings in an urban-like setting, Build. Environ. 169 (2020), 106557.

[79] D.R. Drew, J.F. Barlow, S.E. Lane, Observations of wind speed profiles over Greater London, UK, using a Doppler lidar, J. Wind Eng. Ind. Aerod. 121 (2013) 98–105.

[80] C.W. Kent, C.S.B. Grimmond, D. Gatey, J.F. Barlow, Assessing methods to extrapolate the vertical wind-speed profile from surface observations in a city centre during strong winds, J. Wind Eng. Ind. Aerod. 173 (2018) 100–111.

[81] C. Yuan, E. Ng, Building porosity for better urban ventilation in high-density cities-A computational parametric study, Build. Environ. 50 (2012) 176–189.

[82] V. Cheng, E. Ng, Thermal comfort in urban open spaces for Hong Kong, Architect. Sci. Rev. 49 (3) (2006) 236–242.

[83] E. Ng, C. Chan, V. Cheng, Urban Climatic Map and Standards for Wind Environment - Feasibility Study. Technical Input Report No.1: Methodologies and Findings of User's Wind Comfort Level Survey, Planning Department, Hong Kong, 2008.

[84] E. Ng, C. Yuan, L. Chen, C. Ren, J.C. Fung, Improving the wind environment in high-density cities by understanding urban morphology and surface roughness: a study in Hong Kong, Landsc. Urban Plann. 101 (1) (2011) 59–74.

[85] P. Wang, W.B. Goggins, Y. Shi, X. Zhang, C. Ren, K.K.-L. Lau, Long-term association between urban air ventilation and mortality in Hong Kong, Environ. Res. 197 (2021), 111000.

[86] PlanD, Working Paper 2C: Wind Tunnel Benchmarking Studies - Batch II, Urban Climatic Map and Standards for Wind Environment - Feasibility Study, Planning Department, Hong Kong SAR government (PlanD), Hong Kong, 2010.

[87] T. Gronemeier, K. Surm, F. Harms, B. Leitl, B. Maronga, S. Raasch, Validation of the dynamic core of the PALM model system 6.0 in urban environments: LES and wind-tunnel experiments, Geosci. Model Dev. Discuss. (GMDD) (2020) 1–26.

[88] J. Resler, K. Eben, J. Geletič, P. Krč, M. Rosecký, M. Sühring, M. Belda, V. Fuka, T. Halenka, P. Huszár, Validation of the PALM model system 6.0 in a real urban environment: a case study in Dejvice, Prague, the Czech Republic, Geosci. Model Dev. (GMD) 14 (8) (2021) 4797–4842.

[89] L. Chen, E. Ng, X. An, C. Ren, M. Lee, U. Wang, Z. He, Sky view factor analysis of street canyons and its implications for daytime intra-urban air temperature differentials in high-rise, high-density urban areas of Hong Kong: a GIS-based simulation approach, Int. J. Climatol. 32 (1) (2012) 121–136.